

Envelope Expansion with Core Collapse. III. Similarity Isothermal Shocks in a Magnetofluid

Cong Yu^{1,5}, * Yu-Qing Lou^{2,3,4}, Fu-Yan Bian², and Yan Wu²

¹*National Astronomical Observatories/Yunnan Astronomical Observatory, Chinese Academy of Sciences, Kunming, 650011, China;*

²*Physics Department and Tsinghua Centre for Astrophysics (THCA), Tsinghua University, Beijing, 100084, China;*

³*Department of Astronomy and Astrophysics, the University of Chicago, 5640 South Ellis Avenue, Chicago, IL 60637, USA;*

⁴*National Astronomical Observatories of China, Chinese Academy of Sciences, A20, Datun Road, Beijing 100012, China;*

⁵*Graduate School of the Chinese Academy of Sciences, Beijing, China.*

Accepted 2006 ?? ??. Received 2006 ?? ??; in original form 2005 ?? ??

ABSTRACT

We explore magnetohydrodynamic (MHD) solutions for envelope expansions with core collapse (EECC) with isothermal MHD shocks in a quasi-spherical symmetry and outline potential astrophysical applications of such magnetized shock flows. By including a random magnetic field in a gas medium, we further extend the recent isothermal shock results of Bian & Lou who have unified earlier similarity isothermal shock solutions of Tsai & Hsu, of Shu et al. and of Shen & Lou in a more general framework. MHD shock solutions are classified into three classes according to the downstream characteristics near the core. Class I solutions are those characterized by free-fall collapses towards the core downstream of an MHD shock, while Class II solutions are those characterized by Larson-Penston (LP) type near the core downstream of an MHD shock. Class III solutions are novel, sharing both features of Class I and II solutions with the presence of a sufficiently strong magnetic field as a prerequisite. Various MHD processes may occur within the regime of these isothermal MHD shock similarity solutions, such as sub-magnetosonic oscillations, free-fall core collapses, radial contractions and expansions. Both possibilities of perpendicular and oblique MHD shocks are analyzed. Under the current approximation of MHD EECC solutions, only perpendicular shocks are systematically calculated. These similarity MHD shocks propagate at either sub-magnetosonic or super-magnetosonic constant speeds. We can construct Class I, II and III MHD shocks matching with an isothermal magnetostatic outer envelope or an MHD breeze. We can also construct families of twin MHD shock solutions as well as an ‘isothermal MHD shock’ separating two magnetofluid regions of two different yet constant temperatures. The versatile behaviours of such MHD shock solutions may be utilized to model a wide range of astrophysical problems, including star formation in magnetized molecular clouds, ‘MHD champagne flows’ in HII regions around luminous massive OB stars, MHD link between the asymptotic giant branch phase to the proto-planetary nebula phase with a hot central magnetized white dwarf, relativistic MHD pulsar winds in supernova remnants, radio afterglows of soft gamma-ray repeaters and so forth.

Key words: magnetohydrodynamics (MHD) – radiation mechanisms: general – shock waves – stars: AGB and post-AGB – stars: formation – stars: winds, outflows

1 INTRODUCTION

Many astrophysical processes, including star formation, stellar collapse, supernova explosions, gamma-ray bursts (GRBs) and galaxy cluster evolution etc., may involve self-

gravitational inflows and outflows during a certain phase of evolution. These problems with different approximations (e.g., isothermal or polytropic equations of state, spherical or cylindrical symmetries, radiative or non-radiative regimes etc.) have been explored extensively in various contexts (Bodenheimer & Sweigart 1968; Shu 1977; Goldreich & Weber 1980; Suto & Silk 1988; Foster & Chevalier 1993; Boily & Lynden-Bell 1995; Murakami, Nishihara & Hanawa 2004;

* E-mail: louyq@tsinghua.edu.cn; lou@oddjob.uchicago.edu; yccit@yahoo.com.cn

Shadmehri 2005). When a gas medium has evolved sufficiently far away from the influence of initial and boundary conditions, it may gradually evolve into self-similar behaviours (e.g., Sedov 1959; Landau & Lifshitz 1959; Barenblatt & Zel'dovich 1972). This evolving trend as indicated by numerical calculations to adjust to a roughly self-similar profile led Larson (1969a,b) and Penston (1969a,b) to develop a spherically symmetric isothermal self-gravitating similarity solution which has a flat inner density profile with a radial speed proportional to radius and a supersonic outer envelope with an expansion speed 3.3 times the isothermal sound speed. Shu (1977) constructed an alternative self-similar expansion-wave collapse solution (EWCS), in which the initial condition is an isothermal sphere with a gas mass density $\rho \propto r^{-2}$ throughout in a hydrostatic equilibrium. Perturbations or some central energy loss initiate the collapse and a rarefaction wave front travels outward through the gas medium inside of which gas materials rapidly attain free-fall velocity towards to the centre. This EWCS scenario of inside-out collapse for protostar formation has been advocated by Shu, Adams & Lizano (1987) and compared with observations (Adams, Lada & Shu 1987; Zhou et al. 1993; Choi et al. 1995; Saito et al. 1999; Harvey et al. 2001). Immediately following the analysis of Shu (1977), Hunter (1977) constructed complete isothermal self-similar solutions by going from negative times to positive times and proposed a new matching method to find solutions in density-speed phase diagrams. He found an infinite number of discrete solutions in the ‘complete solution space’. Whitworth & Summers (1985) have further expanded these solutions into two-parameter continua by allowing weak discontinuities across the sonic critical line. Expansion wave solutions for more general adiabatic and self-gravitating gas flows were discussed by Cheng (1978). Suto & Silk (1988) studied generalized polytropic similarity solutions. Yahil (1983) obtained polytropic flow solutions of the Larson-Penston (LP) type with the polytropic index γ in the range of $6/5 < \gamma < 4/3$ for applications to stellar collapse and noted that various solution features appear to be in accordance with results of numerical simulations. Foster & Chevalier (1993) studied the gravitational collapse of an isothermal cloud by hydrodynamic simulations. They recovered the LP solution in the central region where a core forms and the self-similar solution of Shu (1977) when the ratio of initial outer cloud radius to core radius is $\gtrsim 20$.

Shock processes can naturally occur in diverse astrophysical settings, for example, supernova explosions, photoionized gas, stellar winds, collisions between high velocity clumps of interstellar gas, collisions of two or several galaxies etc. Shocks have been under extensive investigations in contexts of supernova remnants (SNRs), nebulae associated with T Tauri stars, planetary nebulae, HII regions, particle accelerations and GRBs etc. (e.g., McKee & Hollenbach 1980; Draine & McKee 1993; Mészáros 2002). McKee & Ostriker (1977) explored the interaction of a SNR with an inhomogeneous ambient medium. Self-similar hydrodynamic shocks were studied for interaction zones of colliding stellar winds (Chevalier 1982; Chevalier & Imamura 1983). Tsai & Hsu (1995) constructed self-similar shocks describing a situation in which a central thermal or kinetic energy release initiates an outgoing shock during a protostellar collapse to form a low-mass star. Tsai & Hsu (1995) also constructed a

shock expansion solution with a finite core density matched with a static SIS envelope; this solution has been generalized into a family of ‘champagne flow’ shock solutions by Shu et al. (2002) to model expansions of HII regions surrounding massive OB stars after a rapid passage of an initial ionization front in a neutral hydrogen cloud. Shen & Lou (2004) studied EECC shock solutions by allowing outflows or in-flows far away from the central region. In terms of modelling protostellar systems, this flexibility can accommodate a variety of physical possibilities. Bian & Lou (2005) explored the parameter space more systematically to construct various isothermal shock solutions, including twin shocks, two temperature shocks and so forth.

Chevalier & Imamura (1982) performed a linear stability analysis for a one-dimensional shock driven by a constant velocity piston. For a radiative cooling function $\Lambda \propto \rho^2 T^\alpha$, they found that radiative shocks were unstable for $\alpha \leq 0.4$ in a fundamental mode and unstable to overtone modes for $\alpha \leq 0.8$. Bertschinger (1986) further extended their work to three dimensions and showed that transverse modes would be unstable for $\alpha \leq 1.0$. Ryu & Vishniac (1987) applied the linear theory to the dynamic instability of strong plane-parallel or spherical adiabatic blast shock waves in a gas medium with an initially uniform density and found that such blast waves to be unstable for an adiabatic index $\gamma \leq 1.2$. Blondin & Cioffi (1989) have shown that local instabilities are restricted to wavelengths less than the shock thickness. Vishniac (1993) examined the dynamical and gravitational instabilities of spherical shocks. Toth & Draine (1993) carried out linear stability analysis as well as numerical simulations to study effects of a transverse magnetic field on magnetohydrodynamic (MHD) shock stability and found that a transverse magnetic field tends to stabilize the flow. MHD shocks in a gas medium of low fractional ionization are subject to a novel dynamical instability involving the deformation of magnetic field lines (Wardle 1990). Decelerating radiative shock fronts (e.g., expanding SNRs in the snowplow phase) are subject to a ripping instability (e.g., Vishniac 1983; Vishniac & Ryu 1989). Drury (1984) noted that acoustic waves propagating towards a shock in the preshock medium may be amplified as they enter a region with a steep cosmic-ray pressure gradient. Rayleigh-Taylor instabilities arise in the cosmic-ray precursor would further complicate the structure of the precursor when the density gradient due to these nonlinear sound waves opposes the cosmic-ray pressure gradient (e.g., Ryu 1993).

Magnetic fields play important roles in various astrophysical environments. Complex filamentary structures in molecular clouds, shapes and shaping of planetary nebulae, synchrotron radiation from SNRs, magnetized stellar winds, galactic winds, GRBs, dynamo effects in stars, galaxies, and galaxy clusters as well as other interesting problems all involve magnetic fields (e.g., Hartmann 1998; Balick & Frank 2002). Due to the formation of filamentary structures in numerical simulations [e.g., Porter et al. (1994); Klessen & Burkert (2000); Ostriker et al. (2001)] and the appearance of numerous filaments in observations (e.g., Falgarone et al. 2001), analyses on processes of filament formation and evolution have also been pursued (Kawachi & Hanawa 1998; Hennebelle 2003; Tilley & Pudritz 2003; Shadmehri 2005). For these reasons, MHD shocks are under extensive investigations. Bazer & Er-

icson (1959) were among the first to study hydromagnetic shocks for astrophysical applications. Whang (1984) studied forward-reverse hydromagnetic shock pairs in the heliosphere. Chakrabarti (1989, 1990) investigated MHD shocks in accretion discs. Numerical simulations were carried out to investigate the spherically symmetric shock interaction of pulsar wind nebula in a SNR (e.g., van der Swaluw et al. 2001). Recently, Del Zanna et al. (2004) re-examined this problem in an axisymmetric geometry. Ouyed & Pudritz (1993) studied oblique MHD shocks in disc winds from young stellar objects (YSOs) to explain broad, blueshifted forbidden emission lines observed in these sources. Duncan & Thompson (1992) proposed very strongly magnetized neutron star might be the origin of soft SGRs and anomalous X-ray pulsars (AXPs). Magnetic fields play an important role in the formation of the three-ring structure around supernova 1987A (e.g., Tanaka & Washimi 2002). Gaensler et al. (2005) found an expanding radio nebula produced by a giant flare from the magnetar SGR 1806-20 and interpreted it as ejecta colliding with pre-existing shells.

In addition to Newtonian shocks, relativistic shocks are also investigated in various contexts. Blandford & McKee (1976) studied relativistic blast wave solutions in spherical geometry and calculate the active galactic nucleus (AGN) radiation spectrum using their blast wave solutions. Kennel & Coroniti (1984) considered ultra-relativistic MHD shock models for the Crab Nebula. Emmering & Chevalier (1987) studied relativistic MHD shocks and applied their results to pulsar winds. Best & Sari (2000) re-examined the problem of Blandford & McKee (1977) and found second-type self-similar solutions to the problem of ultra-relativistic strong explosions. Perna & Vietri (2002) studied the propagation of a relativistic shock in an exponential atmosphere and applied their solutions to GRBs. Nakayama & Shigeyama (2005) reconsidered this problem in a plane-parallel geometry. Hidalgo & Mendoza (2005) considered imploding self-similar relativistic shock waves. Dynamics of relativistic magnetized blast wave was explored by Lyutikov (2002). Takahashi et al. (2002) investigated MHD adiabatic shock accreting onto a rotating Kerr black hole. Subsequently, Fukumura (2004) studied isothermal shock formation around a Kerr black hole. Das et al. (2003) studied isothermal shocks around Schwarzschild black hole using the pseudo-Schwarzschild potential. Mildly magnetized internal relativistic shocks in GRBs have been invoked to explain the GRB prompt emission data (Fan et al. 2004).

The role of a random magnetic field in our model analysis is characterized by an important magnetic parameter λ as defined by equation (5). Different systems of astrophysical objects involve a range of λ values. The estimated λ parameter for the Crab Nebula is of the order of a magnitude around $10^5 \sim 10^6$. For star forming regions, the estimated λ is typically in the range of $0.01 \sim 0.1$. For planetary nebulae, a typical λ is approximately 10^{-3} . For a cluster of galaxies, the estimated λ is approximately 0.2. We would take $\lambda \sim 0.1$ typical for a star formation region for our later discussions. For a star formation cloud, we estimate

$$\lambda \sim 0.1 \left(\frac{B_{\parallel}}{1.34 \times 10^{-4} \text{G}} \right)^2 \left(\frac{\rho}{5 \times 10^{-19} \text{g/cm}^3} \right)^{-2}$$

$$\times \left(\frac{r}{2.24 \times 10^{17} \text{cm}} \right)^{-2}$$

This paper is structured as follows. The basic nonlinear MHD equations and the self-similar MHD transformation are described in Section 2. In Section 3, we present the MHD shock conditions. In Section 4, we solve the nonlinear MHD ordinary differential equations (ODEs) numerically to construct various MHD shock solutions. We provide comments and discussions in Section 5. Relevant technical details of mathematical analyses are summarized in several appendices for the convenience of reference.

2 PHYSICAL ASSUMPTIONS AND BASIC MHD MODEL FORMULATION

For a random tangled magnetic field on small scales, we formulate a large-scale MHD problem under the approximation of quasi-spherical symmetry. In spherical polar coordinates (r, θ, ϕ) , the mass conservation equation is

$$\frac{\partial \rho}{\partial t} + \frac{1}{r^2} \frac{\partial(r^2 \rho u)}{\partial r} = 0, \quad (1)$$

where u is the radial bulk flow speed and ρ is the gas mass density. This mass continuity equation (1) above is equivalent to the following equations, namely

$$\frac{\partial M}{\partial r} = 4\pi \rho r^2, \quad \frac{\partial M}{\partial t} + u \frac{\partial M}{\partial r} = 0, \quad (2)$$

where $M(r, t)$ is the enclosed mass within r at time t . The isothermal radial MHD momentum equation is simply

$$\frac{\partial u}{\partial t} + u \frac{\partial u}{\partial r} = -\frac{a^2}{\rho} \frac{\partial \rho}{\partial r} - \frac{GM}{r^2} - \frac{1}{8\pi \rho} \frac{\partial}{\partial r} \langle B_{\parallel}^2 \rangle - \frac{\langle B_{\perp}^2 \rangle}{4\pi \rho r} \quad (3)$$

where a is the isothermal sound speed, $\mathbf{B}_{\parallel} = (B_{\theta}^2 + B_{\phi}^2)^{1/2}$ stands for the random magnetic field component parallel to the MHD shock front and $-\partial \Phi / \partial r \equiv -GM(r, t)/r^2$ with $\Phi(r, t)$ being the gravitational potential. Here, $\langle B_{\parallel}^2 \rangle$ represents a kind of ensemble average of random magnetic field. In our formulation, some terms involving cross correlations of radial and transverse magnetic field components have been ignored (see Appendix C of Yu & Lou 2005). Under the quasi-spherical symmetry, the Poisson equation relating the gas mass density ρ and the gravitational potential Φ is automatically satisfied. Here in equation (3), we keep the magnetic tension force term that was ignored in equation (3) of Chiueh & Chou (1994).

By taking the electrical conductivity to be infinite (i.e., the ideal MHD approximation or complete frozen-in approximation), we arrive at the following relation

$$B_{\parallel} / (\rho r) = \text{const}, \quad (4)$$

where the right-hand side is a constant of integration. The derivation of equation (4) involves the mass conservation and the transverse components of the magnetic induction equation in the quasi-spherical approximation. For details, we refer the reader to Yu & Lou (2005). Using integral (4), we define the dimensionless parameter λ according to

$$\lambda \equiv B_{\parallel}^2 / (16\pi^2 G \rho^2 r^2) \quad (5)$$

which is a measure for the relative magnitudes of the magnetic energy density and the self gravitational energy density. In comparison with the previous work of Chiueh & Chou (1994), it is apparent that

$$\lambda = \beta(x)/(\alpha^2 x^2), \quad (6)$$

where $\alpha(x)$ and x are the reduced density and the independent similarity variable defined immediately below in equation (7), respectively. Here, variable $\beta(x)$ is a dimensionless function introduced by Chiueh & Chou (1994) and stands for the reduced magnetic pressure, or equivalently, the reduced magnetic energy density. With this comparison, we know from their equation (11) that while our formulation differs from theirs in several aspects, the final magnetosonic critical conditions are in fact identical. The ratio of the Alfvén wave speed v_A to the isothermal sound speed a is given by

$$\frac{v_A}{a} = \left(\frac{\beta}{\alpha}\right)^{1/2} \quad \text{with} \quad v_A \equiv \frac{B_{\parallel}}{(4\pi\rho)^{1/2}}.$$

The dimensionless independent similarity variable is defined by $x \equiv r/(at)$ and the self-similar MHD transformation are

$$\begin{aligned} \rho(r, t) &= \frac{\alpha(x)}{4\pi G t^2}, \quad M(r, t) = \frac{a^3 t}{G} m(x), \quad u(r, t) = a v(x), \\ \Phi(r, t) &= a^2 \phi(x), \quad B_{\parallel}(r, t) = \frac{ab(x)}{\sqrt{G}t}, \end{aligned} \quad (7)$$

where the dimensionless $\alpha(x)$, $m(x)$, $v(x)$, $\phi(x)$ and $b(x)$ are the reduced dependent variables for the mass density, the enclosed mass, the radial flow speed, the gravitational potential and the transverse magnetic field strength, respectively; and they are all dimensionless functions of x only. Note that $b(x) = \sqrt{\lambda}\alpha x$ and is related to the dimensionless function $\beta(x)$ of Chiueh & Chou (1994) by $b^2 \equiv \beta$.

It follows that equations (2) reduce to

$$m' = x^2 \alpha, \quad (v - x)m' + m = 0, \quad (8)$$

where the prime denotes the derivative with respect to x . Combining these two ODEs, we immediately obtain the following two equations

$$m = (x - v)x^2 \alpha, \quad [x^2 \alpha(x - v)]' = x^2 \alpha. \quad (9)$$

By equation (9), the physical requirement of a positive enclosed mass $m(x) > 0$ is equivalent to the condition $x - v > 0$. Thus, solutions of v must lie to the upper-right of the straight line $x - v = 0$ in the plane $-v(x)$ versus x .

After substituting the self-similar variables into continuity and momentum equations, we derive the following two coupled nonlinear MHD ODEs

$$\begin{aligned} [(x - v)^2 - (1 + \lambda \alpha x^2)] v' \\ = (x - v) [\alpha(x - v) - 2/x], \end{aligned} \quad (10)$$

$$\begin{aligned} [(x - v)^2 - (1 + \lambda \alpha x^2)] \alpha' / \alpha \\ = (x - v) [\alpha - 2(x - v)/x] + 2\lambda x \alpha. \end{aligned} \quad (11)$$

Setting $\lambda = 0$ for the absence of the magnetic field, we readily recover the hydrodynamic formulation of Lou & Shen (2004). In the above two coupled nonlinear MHD ODEs (10) and (11), the magnetosonic critical curve is specified by

$$x - v = 2/(\alpha x) \quad \text{and} \quad x - v + 2\lambda x = (x - v)^3. \quad (12)$$

Note that for $\lambda = 0$ and $x - v > 0$, equation (12) becomes $x - v = 1$ and $\alpha = 2/x$. Given the positiveness of $x - v > 0$, we come to the familiar condition $x - v = 1$ for the isothermal sonic critical line (Lou & Shen 2004). Equation $(x - v)^2 = 1 + \lambda \alpha x^2$ is equivalent to the equation $(x - v)^2 = (a^2 + v_A^2)/a^2$, directly related to the fast magnetosonic condition as anticipated on the ground of physics.

The asymptotic MHD solution behaviours of the coupled nonlinear MHD ODEs are summarized below. As MHD generalizations, these asymptotic solutions were derived in parallel to hydrodynamic results (see Appendix A of Lou & Shen 2004 for more details of their derivations). We emphasize that there is no hydrodynamic counterpart for class III asymptotic solutions as $x \rightarrow 0^+$ described below. In addition to $v(x)$ and $\alpha(x)$, we also provide corresponding asymptotic solutions of $\beta(x)$ for the reduced magnetic pressure for relevant physical information and a more complete presentation.

In the limit of $x \rightarrow +\infty$, we have asymptotic solutions

$$\begin{aligned} v(x) &= V + \frac{2 - A}{x} + \frac{V}{x^2} \\ &+ \frac{(A/6 - 1)(A - 2) + 2V^2/3 + A(2 - A)\lambda/3}{x^3} + \dots, \end{aligned} \quad (13)$$

$$\begin{aligned} \alpha(x) &= \frac{A}{x^2} + \frac{A(2 - A)}{2x^4} + \frac{A(4 - A)V}{3x^5} + \\ &+ \frac{A(A - 3)(A/2 - 1) - (A - 6)AV^2/4 + (2 - A)A^2\lambda/4}{x^6} \\ &+ \dots, \end{aligned} \quad (14)$$

$$\begin{aligned} \beta(x) &= \lambda \alpha^2 x^2 = \frac{A^2 \lambda}{x^2} + \frac{A^2(2 - A)\lambda}{x^4} + \frac{A^2(2 - A)^2 \lambda}{4x^6} \\ &+ \dots, \end{aligned} \quad (15)$$

where A and V are two constants of integration mainly for mass density and radial flow speed, respectively.

Class I: For a central MHD free-fall collapse in the limit of $x \rightarrow 0^+$, we have to the leading order

$$v = -2F/x^{1/2} - \frac{3}{4F}x^{1/2} \ln x - 2Lx^{1/2} + \dots, \quad (16)$$

$$\alpha = F/x^{3/2} - \frac{3}{8F}x^{-1/2} \ln x - Lx^{-1/2} + \dots, \quad (17)$$

$$\beta = \lambda \alpha^2 x^2 = \frac{\lambda F^2}{x} + \dots, \quad (18)$$

where F and L are two constants of integration.

Class II: For the central LP-type MHD solutions being regular as $x \rightarrow 0^+$, we have

$$v = \frac{2}{3}x + \frac{(2 - 3D - 18D\lambda)}{135}x^3 + \dots, \quad (19)$$

$$\alpha = D + \frac{D(2 - 3D - 18D\lambda)}{18}x^2 + \dots, \quad (20)$$

$$\beta = \lambda \alpha^2 x^2 = \lambda D^2 x^2 + \dots, \quad (21)$$

where D is an integration constant.

Class III: There exists a novel class of asymptotic MHD solutions which requires a sufficiently strong magnetic field and would disappear in the absence of magnetic field. As $x \rightarrow 0^+$, we write to the leading order

$$v(x) = Hx + \dots, \quad (22)$$

$$\alpha(x) = K/x^\eta + \dots, \quad (23)$$

where K is an arbitrary integration constant and

$$H = [2 - \lambda \pm (\lambda^2 - 4\lambda)^{1/2}]/2 < 0, \quad (24)$$

$$\eta = (1 - H + 2\lambda)/\lambda \quad \text{with} \quad 2 \leq \eta \leq 3. \quad (25)$$

It is then straightforward to infer that as $x \rightarrow 0^+$,

$$\beta(x) = \lambda \alpha^2 x^2 \rightarrow \frac{\lambda K^2}{x^{2(\eta-1)}}, \quad (26)$$

$$B_\parallel^2 \rightarrow \frac{\lambda K^2 a^{2\eta} t^{2(\eta-2)}}{Gr^{2(\eta-1)}}. \quad (27)$$

For this new class of asymptotic MHD solutions, the magnetic field strength scales as $B_\parallel \propto r^{-(\eta-1)}$ at a fixed moment t , while at a given radius r , we have the scaling $B_\parallel \propto t^{\eta-2}$. The power index η is such that $-2 \leq -(\eta-1) \leq -1$. By expression (24), this type of MHD solutions exists only when the magnetic parameter λ is greater than 4.

It is possible for similarity MHD solutions to go across the magnetosonic critical curve smoothly. Along the magnetosonic critical curve (e.g., Jordan & Smith 1977), the two MHD eigensolutions are governed by the following quadratic equation with $z \equiv v'$, namely

$$\left[(v-x) - \frac{x\lambda}{(v-x)^2} \right] z^2 + (x-v)z - \frac{v}{x^2} = 0. \quad (28)$$

From equation (28), we obtain two types of MHD eigensolutions for $z \equiv v'$ along the magnetosonic critical curve. When the two roots of equation (28) are of opposite signs, type 1 and type 2 eigensolutions are those with negative and positive roots of equation (28), respectively. When the two roots of equation (28) are of the same sign, type 1 and 2 eigensolutions are those with smaller and larger absolute values respectively. In the open interval $0 < x < 2$, type 1 and type 2 are exactly defined as such. When $x > 2$ (relevant to the LP-type MHD solution), dv/dx of type 1 has a larger absolute value, while dv/dx of type 2 has a smaller absolute value; that is, their magnitudes reverse for nodal points. In our current definition, no magnitude reversal would happen. When the point is a nodal point, type 1 and type 2 solutions remain always the smaller and larger ones respectively for the absolute value of dv/dx . To summarize, our definition is not defined by the explicit expressions of dv/dx (e.g., $1 - 1/x_*$ and $1/x_*$), but by their magnitudes and signs. It is easier to keep in mind their relevant physical properties.

3 ISOTHERMAL MHD SHOCK CONDITIONS

3.1 Perpendicular MHD Shock

3.1.1 The One-Temperature Case

The simplest type of MHD shock wave is the perpendicular shock. In this case, the velocities of both the shock and plasma are perpendicular to the magnetic field, which itself is parallel to the shock front. In a frame of reference moving with the MHD shock front, the properties on both sides of the shock (ρ_1, u_1, B_1, p_1) and (ρ_2, u_2, B_2, p_2) are related by the equations for conservation of mass, momentum, energy and magnetic flux. In the isothermal approximation, we need not to consider the MHD energy equation.

In dimensional form, the perpendicular MHD shock conditions are (e.g., Priest 1982)

$$\rho_2 u_2 = \rho_1 u_1, \quad (29)$$

$$p_2 + B_2^2/(8\pi) + \rho_2 u_2^2 = p_1 + B_1^2/(8\pi) + \rho_1 u_1^2, \quad (30)$$

$$B_2 u_2 = B_1 u_1. \quad (31)$$

In equation (30), the term $B^2/(8\pi)$ represents the magnetic pressure. In equation (31), the quantity Bv gives the rate at which the magnetic flux is transported across a unit surface area; physically, this quantity is actually proportional to the electric field component tangential to the shock front and thus should remain continuous across a shock. After straightforward manipulations, the solution to the above set of MHD shock equations can be expressed in terms of the mass density ratio $\rho_2/\rho_1 \equiv X$, the upstream Mach number $M_1 \equiv u_1/a$, and the upstream plasma beta parameter¹ $\beta_1 \equiv p_1/(B_1^2/8\pi) = 2a^2/v_{A1}^2$. The results are simply

$$u_2/u_1 = 1/X,$$

$$B_2/B_1 = X,$$

$$p_2/p_1 = X,$$

where X is the positive root of the following quadratic equation (see Appendix A for detailed derivations)

$$f(X) = X^2 + (\beta_1 + 1)X - \beta_1 M_1^2 = 0; \quad (32)$$

this equation readily indicates the existence of only one positive root of X . Physically, we should further require $X > 1$ for a fast magnetosonic shock.

When upstream conditions are specified, we can determine the downstream conditions behind a magnetosonic shock systematically. We simply take ρ_2 as ρ_d and ρ_1 as ρ_u such that

$$u_2 = u_d - u_s, \quad u_1 = u_u - u_s,$$

$$u_u = av_u, \quad u_d = av_d, \quad u_s = ax_s,$$

$$X = \rho_2/\rho_1 = \rho_d/\rho_u,$$

where u_s is the radial shock speed, and subscripts u and d denote physical variables associated with upstream and downstream sides, respectively. It then follows that

$$\alpha_d/\alpha_u = X,$$

$$(v_d - x_s)/(v_u - x_s) = 1/X,$$

$$M_1 = v_u - x_s,$$

$$\beta_1 = 2/(\lambda x_s^2 \alpha_u).$$

Here, the value of X should be larger than 1 for a magnetosonic shock – a kind of MHD fast shock.

The analysis of quadratic equation (32) shows that the two real roots of X have opposite signs. We naturally pick out the positive root among the two.

When $f(X=1) < 0$, i.e., $2 + \beta_1 < \beta_1 M_1^2$ or $1 + 2/\beta_1 < M_1^2$, it has a positive root $X > 1$. This conclusion can also be reached by directly solving the quadratic equation and

¹ We emphasize here that β_1 is the upstream plasma parameter, not the dimensionless $\beta(x)$ function for the reduced magnetic pressure defined in the previous context (see equation 6).

by requiring the positive root $X > 1$. Physically for a magnetosonic shock to exist, the upstream flow speed relative to the shock speed must exceed the upstream fast magnetosonic speed $(a^2 + v_{A1}^2)^{1/2}$. This serves as a guide in constructing magnetosonic shocks.

When $f(X = 1) > 0$, i.e., $2 + \beta_1 > \beta_1 M_1^2$ or $1 + 2/\beta_1 > M_1^2$, there is a positive root $X < 1$.

Using the definitions of β_1 and M_1 in the condition $1 + 2/\beta_1 = M_1^2$ and dropping the subscript 1, this equation describes exactly the behaviour of the magnetosonic critical curve $(x - v)^2 = 1 + \lambda \alpha x^2$.

3.1.2 Two-Temperature MHD Shocks

When the constant temperatures on the two sides of a magnetosonic shock are different, we have the following two MHD jump conditions in the shock framework of reference

$$\alpha_d(v_d - x_{sd})a_d = \alpha_u(v_u - x_{su})a_u, \quad (33)$$

$$a_d^2[\lambda \alpha_d^2 x_{sd}^2/2 + \alpha_d + \alpha_d(v_d - x_{sd})^2] = a_u^2[\lambda \alpha_u^2 x_{su}^2/2 + \alpha_u + \alpha_u(v_u - x_{su})^2]. \quad (34)$$

When the upstream conditions are given and we are going to determine the downstream conditions, we take ρ_2 as ρ_d and ρ_1 as ρ_u . It then follows that

$$a_d/a_u = \tau, \quad x_{sd}/x_{su} = 1/\tau, \quad (35)$$

$$\alpha_d/\alpha_u = (v_u - x_{su})/[\tau(v_d - x_{sd})] = X, \quad (36)$$

$$\beta_1 = 2/(\lambda x_{su}^2 \alpha_u), \quad (37)$$

$$X^2/\beta_1 + \tau^2 X + M_1^2/X = 1/\beta_1 + 1 + M_1^2. \quad (38)$$

Equation (38) is a cubic equation in terms of X , namely

$$f(X) \equiv X^3 + \beta_1 \tau^2 X^2 - (1 + \beta_1 + \beta_1 M_1^2)X + \beta_1 M_1^2 = 0. \quad (39)$$

For a physical magnetosonic shock solution, we should require both $\tau > 1$ and $X > 1$. In constructing magnetosonic shock solutions, we then choose the positive root(s) $X > 1$ among the three roots of cubic equation (38) for X . Since $f(X = 1) = \beta_1(\tau^2 - 1) > 0$ and $f(X = 0) = \beta_1 M_1^2 > 0$, cubic equation (38) must have at least one negative X root because $f(-\infty) = -\infty$ and $f(+\infty) = +\infty$. The remaining two roots could be either both complex or both real. When the other two roots are either complex roots or both less than 1, there is no magnetosonic shock solution. When these other two real X roots are both larger than 1, there exist two possible magnetosonic shock solutions. From equation (39), we derive $f'(X) \equiv df/dX$ as

$$f'(X) = 3X^2 + 2\beta_1 \tau^2 X - (1 + \beta_1 + \beta_1 M_1^2). \quad (40)$$

According to expression (40), the two real roots (one positive X_+ and the other negative X_-) of $f'(X) = 0$ are given by

$$X_{\pm} = \{-\beta_1 \tau^2 \pm [\beta_1^2 \tau^4 + 3(1 + \beta_1 + \beta_1 M_1^2)]^{1/2}\}/3. \quad (41)$$

By definition (39) for $f(X)$ and the fact of $f(X = 0) = \beta_1 M_1^2 > 0$, it is clear that $f(X_-)$ should remain positive. For the situation of $f(X_+) > 0$, the two remaining roots form a complex conjugate pair and there is no magnetosonic shock solution. For the situation of $f(X_+) \leq 0$, the two remaining roots are real and positive. It is found that if the two roots are real only two situations can happen: (i) the two roots

are both positive and less than 1; and (ii) the two roots are both larger than 1. The situation that one root is greater than 1 and the other positive root is less than 1 cannot occur because this would demand $f(X = 1) < 0$.

We have just analyzed several solution properties of the cubic equation for the mass density ratio X given upstream physical conditions of a magnetosonic shock. However, in practical calculations, we did not search for root $X > 1$ using the above procedure with $\tau > 1$. We adopted an alternative yet equivalent procedure described below. In fact, our later two-temperature calculations are performed with the following procedure involving one root of an equivalent cubic equation.

Reciprocally, when downstream conditions are given, we can calculate the upstream conditions across a magnetosonic shock. Under this situation, we simply take ρ_2 as ρ_u and ρ_1 as ρ_d and so forth. It then follows that

$$\frac{a_u}{a_d} = \tilde{\tau}, \quad \frac{x_{su}}{x_{sd}} = \frac{1}{\tilde{\tau}}, \quad (42)$$

$$\frac{\alpha_u}{\alpha_d} = \frac{(v_d - x_{sd})}{\tilde{\tau}(v_u - x_{su})} = \tilde{X}, \quad (43)$$

$$\tilde{M}_1 = v_d - x_{sd},$$

$$\tilde{\beta}_1 = 2/(\lambda x_{sd}^2 \alpha_d),$$

$$\tilde{X}^2/\tilde{\beta}_1 + \tilde{\tau}^2 \tilde{X} + \tilde{M}_1^2/\tilde{X} = 1/\tilde{\beta}_1 + 1 + \tilde{M}_1^2. \quad (44)$$

This is a cubic equation in \tilde{X} of exactly the same mathematical form as equation (39), namely

$$f(\tilde{X}) = \tilde{X}^3 + \tilde{\beta}_1 \tilde{\tau}^2 \tilde{X}^2 - (1 + \tilde{\beta}_1 + \tilde{\beta}_1 \tilde{M}_1^2)\tilde{X} + \tilde{\beta}_1 \tilde{M}_1^2 = 0. \quad (45)$$

For a physical magnetosonic shock, we naturally require $\tilde{\tau} < 1$ and $\tilde{X} < 1$. In numerical calculations, we choose the positive \tilde{X} root that is less than 1 among the three roots of cubic equation (45). It turns out to be much simpler in analyzing this cubic equation. Because here $f(\tilde{X} = 1) = \tilde{\beta}_1(\tilde{\tau}^2 - 1) < 0$ and $f(\tilde{X} = 0) = \tilde{\beta}_1 \tilde{M}_1^2 > 0$, this cubic equation must then have three real roots, one negative and two positive. One positive root is larger than 1 and the other positive root is smaller than 1. In comparison with the cases of $\tau > 1$ in equation (39), there is only one \tilde{X} root of cubic equation (45) physically corresponding to a magnetosonic shock solution. That the roots of the $\tau > 1$ cases in equation (39) are more complex is related to the fact that $f(X = 1) = \beta_1(\tau^2 - 1) > 0$. Fortunately, in our specific model calculations, we just compute the $\tilde{\tau} < 1$ cases and the amount of our numerical computations can be greatly reduced.

We have also considered the case of oblique MHD shocks in more details (not completely shown here) and find that oblique MHD shocks do not exist in our current model framework. The main reason that we cannot have oblique MHD shocks in our formalism is related to the frozen-in condition (4). Thus from the two following shock relations for an oblique MHD shock (Priest 1982)

$$\frac{B_{2y}}{B_{1y}} = \frac{(u_1^2 - v_{A1}^2)X}{(u_1^2 - Xv_{A1}^2)}$$

and

$$X = \frac{\rho_2}{\rho_1},$$

together with $B_{\parallel} \propto \rho$, we come to the conclusion that

$$\frac{(v_1^2 - v_{A1}^2)X}{(v_1^2 - Xv_{A1}^2)} = X.$$

There is only a trivial solution with $X = 1$. From now on, we ignore the radial magnetic field component and just consider perpendicular MHD shocks.

4 SELF-SIMILAR ISOTHERMAL MHD SHOCK SOLUTIONS

In this section, we present and discuss properties of semi-complete global solutions with perpendicular MHD shocks.

4.1 Extensions of Previous Shock Results by Including a Random Magnetic Field

With the inclusion of a random magnetic field, we can extend previous hydrodynamic similarity shock solutions. More specifically, we would extend the results of Tsai & Hsu (1995), Shu et al. (2002) and Shen & Lou (2004). For a random magnetic field, we envision a simple ‘‘ball of thread’’ scenario in a huge spatial volume of gas medium. A magnetic field line follows the ‘thread’ meandering within a thin spherical ‘layer’ in space in a random manner. In the strict sense, there is always a random weak radial magnetic field component such that random magnetic field lines in adjacent ‘layers’ are actually connected throughout in space. By taking a large-scale ensemble average of such a magnetized system, we are then left with ‘layers’ of random magnetic field components transverse to the radial direction. Very recently, Bian & Lou (2005) carried out extensive investigations on self-similar isothermal shock solutions in the absence of magnetic field, while under the approximation of a quasi-spherical symmetry in the sense described above, Yu & Lou (2005) constructed smooth self-similar isothermal MHD solutions involving a random magnetic field but without shocks. To a greater extent, our present investigation is to combine the analyses of Bian & Lou (2005) and Yu & Lou (2005) as well as to explore new possibilities associated with magnetic field.

4.1.1 MHD Extensions for Shocks of Tsai & Hsu

Alternative to the results of Larson (1969a, b) and Penston (1969a, b), Shu (1977) constructed the EWCS and developed an inside-out collapse scenario for the process of forming low-mass protostars (e.g., Shu et al. 1987). Tsai & Hsu (1995) considered a self-similar shock travelling into a static SIS envelope characterized by $\tau = 1$, $x_{sd} = x_{su} = x_s$, $v_u = 0$ and $\alpha_u = 2/x_s^2$. Their shock connection condition becomes $v_d = x_s - 1/x_s$ and $\alpha_d = 2$ (see their equation 16). Their global shock solutions have different asymptotic behaviours near the origin (see their fig. 6). The diverging free-fall solution near the origin is the Class I solution. The converging LP-type solution near the origin is the Class II solution. In our formalism, we can generalize the shock results of Tsai & Hsu (1995) by incorporating a random magnetic field. When a magnetic field is included, the MHD Class I shock solution generalizing that of Tsai & Hsu (1995) crosses the magnetosonic critical curve at $x_* = 0.0369$ with the shock location at $x_s = 1.3599$ for an outgoing MHD shock front

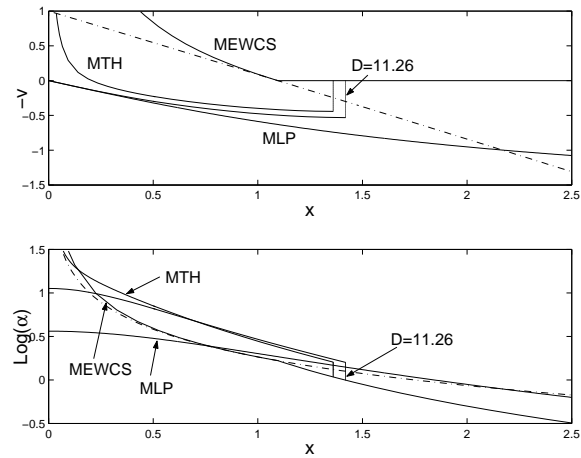


Figure 1. The MHD case of $\lambda = 0.1$. The MHD extensions of Tsai & Hsu (MTH) type similarity shock solutions (Class I MHD shock with free-fall diverging behaviour near the origin and Class II MHD shock with a finite reduced density near the origin and an eigenvalue $D = 11.26$). The negative reduced radial velocity $-v(x)$ (upper panel) and the reduced density $\alpha(x)$ in logarithmic scale (lower panel) versus x in linear scale are shown respectively. MHD Expansion-Wave Collapse Solution (MEWCS) as well as MHD LP (MLP) solution are also displayed. Dash-dotted line represents the magnetosonic critical curve. Class I MHD Tsai & Hsu (MTH) type similarity shock location is at $x_s = 1.3599$ and this solution passes through the magnetosonic critical curve at $x_* = 0.0369$. Class II MHD Tsai & Hsu (MTH) type similarity shock location is at $x_s = 1.4194$.

travelling at a constant speed of 1.3599 times the isothermal sound speed a . The corresponding central mass accretion rate is 0.0726. For the MHD Class II shock solution, a central expansion with a finite central density (LP-type solution) matches with a magnetostatic SIS envelope across an MHD shock. The shock is located at $x_s = 1.4194$ and thus shows a higher shock speed of 1.4194 times the isothermal sound speed a and a reduced core density $D = 11.26$ [see asymptotic solutions (19), (20), and (21)]. In Figure 1 and Figure 2, we plot the MHD extensions of Tsai & Hsu type self-similar shocks. Note that these MHD generalizations of Tsai & Hsu shock solutions are just two special cases among magnetized similarity shock solutions into a magnetostatic SIS envelope. Details of the procedure for constructing these MHD shock solutions will be discussed in section 4.2.

4.1.2 MHD Extensions for Shock Solutions of Shu et al.

Shu et al. (2002) extended the Class II shock solution of Tsai & Hsu (1995) and used these solutions to model ‘champagne flows’ of HII regions surrounding massive OB stars. In a similar manner, by varying the D and x_s parameters with $V = 0$ and a fixed λ , MHD extensions for shock solutions of Shu et al. (2002) are also constructed and presented in Figure 3 and Figure 4. Here the parameters D , V , λ and A , K and H in later discussion are all integration constants in asymptotic solutions (13) to (23). Both the shock speed and shock strength increase with a decreasing D parameter. In the limit of $D \rightarrow 0^+$ numerically, the mass parameter A approaches 0^+ accordingly and the reduced radial speed $v(x)$ converges to an invariant form (Shu et al. 2002; Shen

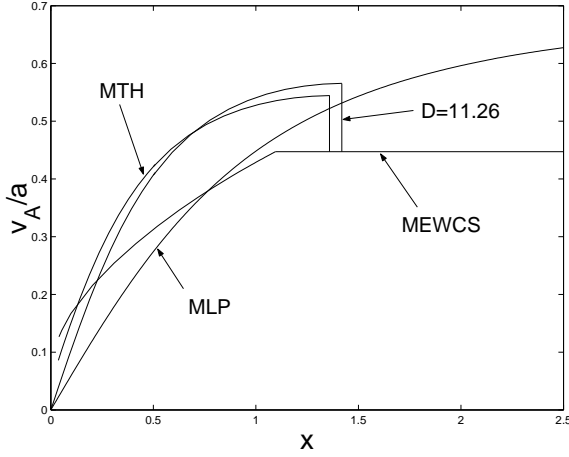


Figure 2. The MHD case of $\lambda = 0.1$. The MHD extensions of Tsai & Hsu (MTH) type similarity shock solutions. The ratio of Alfvén wave speed to the isothermal sound speed v_A/a versus x is shown in linear scales. MHD Expansion-Wave Collapse Solutions (MEWCSs) and MHD LP (MLP) shock solutions are displayed.

& Lou 2004) with an invariant fastest and strongest MHD shock located at $x_s = 2.56$. In other words, as $D \rightarrow 0^+$ numerically, behaviours of the MHD shock solutions gradually become the same as those of the hydrodynamic shock solutions, and for the same parameter D , the MHD shock speeds are faster than the hydrodynamic shock speeds. These shock solutions are MHD generalizations of ‘champagne breezes’ (see curves in our Fig. 3 and the heavy solid curve in our Fig. 7 and compare with fig. 1 of Shu et al. 2002). In Table 1, we summarize properties of the displayed shock solutions in the semi-complete space $0 < x < +\infty$.

Details of the procedure for finding these semi-complete self-similar MHD shock solutions will be discussed presently in section 4.3.

4.1.3 MHD Extensions for Shock Solutions of Shen & Lou

Shen & Lou (2004) further extended the Class I shock solutions by matching with various asymptotic flows and modelled the dynamical evolution of young stellar objects such as Bok globule B335 system to account for the observationally inferred mass density and flow speed profiles as well as the estimated central mass accretion rate. When a random magnetic field is included, MHD extensions for this type of shock solution can also be constructed. The downstream side of such an MHD shock is part of the first type 2-type 1 solution, i.e., the MHD EECC solution (MEECC; Yu & Lou 2005) which crosses the magnetosonic critical curve analytically. The two magnetosonic critical points are at $x_*(1) = 0.103$ and $x_*(2) = 1.811$, respectively. By choosing different shock locations $x_s = 0.4, 0.9, 1.5018, 1.57$ as in Figure 5 and Figure 6, we readily construct various upstream MHD solutions as $x \rightarrow +\infty$. Magnetized ‘champagne flows’ of HII regions around massive OB stars can also be constructed by allowing for MHD flows at large x . Specific examples of such solutions are presented in Figure 7 and Figure 8. Here, the upstream flows are not necessarily limited to a static magnetized SIS envelope or magnetized ‘champagne breezes’ with $V = 0$. With different MHD shock locations or speeds, Class II sim-

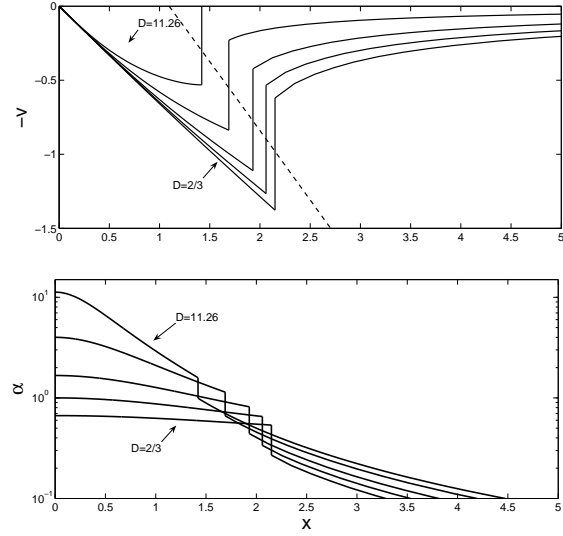


Figure 3. The MHD generalization for similarity shock solutions of Shu et al. (2002) with $\lambda = 0.1$. For self-similar MHD shock solution curves from bottom to top, $D = 2/3, 1, 1.67, 4, 11.26$, respectively. The negative reduced radial speed $-v(x)$ in linear scale (upper panel) and the reduced mass density $\alpha(x)$ in logarithmic scale (lower panel) versus x in linear scale. Both the MHD shock speed and strength increase with a decreasing D parameter. As D approaches 0^+ , the reduced speed $v(x)$ converges to an invariant form with an invariant fastest and strongest shock located at $x_s = 2.56$ (see also the heavy solid curve in Fig. 7). Dashed line represents the magnetosonic critical curve.

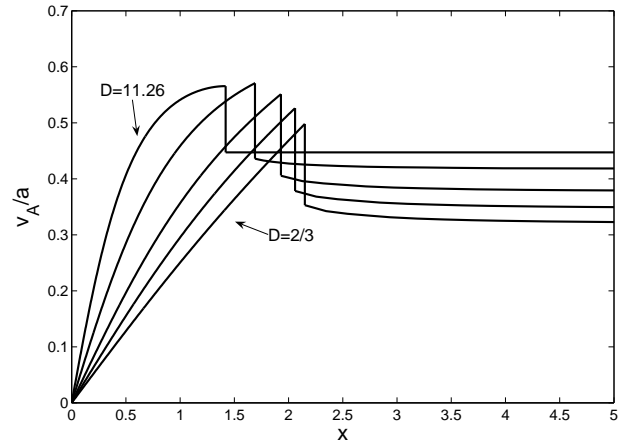


Figure 4. MHD extensions for similarity shock solutions of Shu et al. (2002) with $\lambda = 0.1$. The ratio of Alfvén wave speed and isothermal sound speed v_A/a versus x is shown. Both the shock speed and strength increase with a decreasing D parameter.

ilarity MHD solutions can be matched with either asymptotic MHD outflows ($V > 0$) or asymptotic MHD inflows ($V < 0$).

4.2 MHD Similarity Shocks into

Table 1. MHD Extensions for Shocks of Shu et al. (2002) with $\lambda = 0.1$.

description	A	x_s	v_d	α_d	v_u	α_u
$D = 11.26$	2.00	1.42	0.532	1.59	0	0.992
$D = 4$	1.74	1.69	0.837	1.14	0.230	0.666
$D = 1.67$	1.42	1.93	1.11	0.816	0.423	0.441
$D = 1$	1.20	2.06	1.27	0.653	0.534	0.337
$D = 2/3$	1.02	2.15	1.38	0.537	0.620	0.269
$D = 10^{-5}$	4.30×10^{-5}	2.56	1.91	2.10×10^{-5}	1.02	8.80×10^{-6}
$D = 10^{-6}$	4.30×10^{-6}	2.56	1.91	2.10×10^{-6}	1.02	8.80×10^{-7}

These solutions can be viewed as Class II similarity MHD shock solutions matched with asymptotic MHD breezes. Columns 1 to 7 provide relevant parameters for MHD shock solutions: D is the key parameter in the LP-type asymptotic MHD solutions (19), (20) and (21) at small x ; A is the upstream mass density parameter; x_s indicates either MHD shock location or MHD shock speed; v_d is the reduced speed downstream of an MHD shock; α_d is the reduced density downstream of an MHD shock; v_u is the reduced speed upstream of an MHD shock; and α_u is the reduced density upstream of an MHD shock.

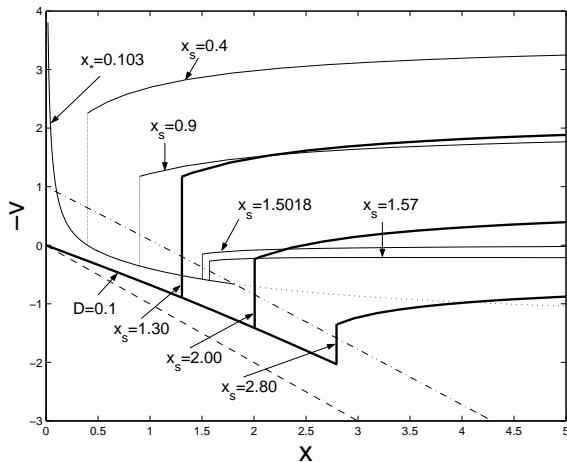


Figure 5. The first MHD EEECC (MEECC) solution with $\lambda = 0.1$ crossing the magnetosonic critical curve analytically at $x_*(1) = 0.103$ and $x_*(2) = 1.811$ [within $x_*(2)$ is light solid curve, while outside $x_*(2)$ is dotted curve]. The light solid curves represent Class I MHD shock solutions with the downstream as part of the first MEECC solution and with shock location x_s at 0.4, 0.9, 1.5018, 1.57, respectively; the heavy solid curves represent Class II MHD shock solutions with the reduced mass density of the central core $D = 0.1$ and with the MHD shock location x_s at 1.30, 2.00, 2.80, respectively. Dash-dotted line represents magnetosonic critical curve. Dashed line is the mass demarcation line $x - v = 0$.

a Magnetostatic SIS Envelope

MHD extensions for shock solutions of Tsai & Hsu (1995) shown earlier are just two cases of our following similarity MHD shock solutions into a magnetostatic SIS envelope. In Tsai & Hsu (1995) and Shu et al. (2002), two classes of shock solutions were constructed to match with a static SIS envelope with $V = 0$ and $A = 2$ or $A < 2$. In Bian & Lou (2005), hydrodynamic shock solutions of Class I and Class II were extensively explored to match with a static SIS envelope. One can also follow the procedure of Hunter to derive the Class I and Class II MHD shock solutions in a parallel manner. Here, we would systematically explore the Class I and Class II MHD shock solutions matched with a magnetostatic SIS envelope by surveying possible solutions

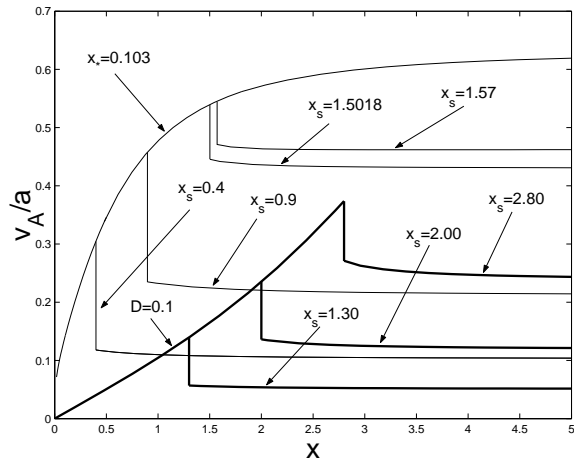


Figure 6. The ratio of the Alfvén wave speed to the isothermal sound speed v_A/a versus x with $\lambda = 0.1$ corresponding to the case of Fig. 5. The light solid curves represent Class I MHD shock solutions with the downstream as part of the first MEECC solution and with the shock location x_s at 0.4, 0.9, 1.5018, 1.57, respectively; the heavy solid curves represent Class II MHD shock solutions with the reduced mass density of the central core $D = 0.1$ and with the MHD shock location x_s at 1.30, 2.00, 2.80, respectively.

in the speed-density phase diagram of v and α . In Figure 10, we present the Class I MHD shock solutions. In Figure 14, we provide the Class II MHD shock solutions. In Table 2, we summarize relevant parameters of the first three MHD shock solutions of both Class I and Class II.

We first consider Class I MHD shock solutions with an outer magnetostatic SIS envelope, having downstream solutions diverging towards the centre and upstream solutions of mass parameter $A = 2$. Tsai & Hsu (1995) obtained a hydrodynamic shock solution for such a case. Bian & Lou (2005) systematically extended the shock results of Tsai & Hsu (1995) and obtained a wide variety of similarity shock solutions. We shall fully explore the speed-density phase diagram for constructing semi-complete MHD shock solutions. For every assigned value for $x_*(1)$ [$x_*(1) < x_m$ where x_m is a chosen meeting point] and after integrating towards the

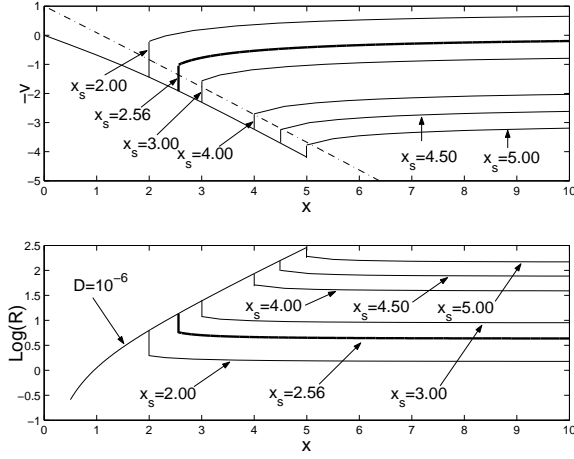


Figure 7. The case of $\lambda = 0.1$. The negative reduced radial speed $-v(x)$ (upper panel) and the scaled reduced mass density $R(x) \equiv x^2 \alpha(x)/D$ (lower panel) versus x . The solid curves form the family of Class II MHD shock solutions in the invariant form with the reduced mass density of the central core $D \rightarrow 0^+$; the heavy solid curve is the MHD shock ‘champagne breeze’ solution. Dash-dotted curve in the upper panel is the magnetosonic critical curve.

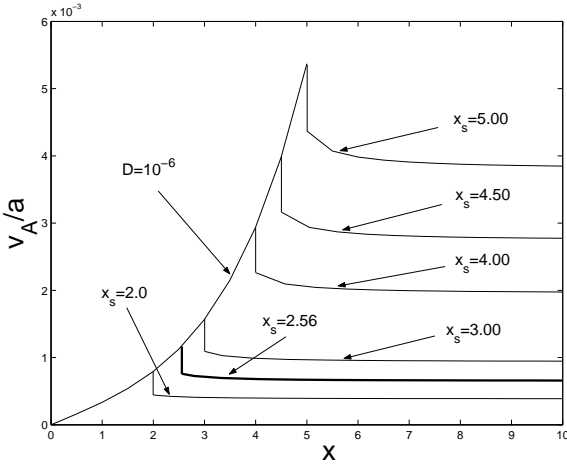


Figure 8. The ratio of the Alfvén wave speed to the isothermal sound speed v_A/a versus x with $\lambda = 0.1$, corresponding to MHD shock solutions in Fig. 7.

meeting point x_m with a type 2 MHD eigensolution, we obtain a pair of $\{v, \alpha\}$ at the meeting point x_m in the so-called phase diagram of v versus α . For a sequence of such $x_*(1)$ values, a series of $\{v, \alpha\}$ pairs is obtained, giving rise to a curve in the phase diagram. The upstream is part of a MEWCS. By choosing an MHD shock location $x_s > x_m$, we determine the corresponding upstream values v_u and α_u at x_s along the MEWCS solution. We then calculate v_d and α_d using the isothermal MHD shock conditions in terms of the upstream values v_u and α_u . Starting from v_d and α_d at x_s , we then integrate the coupled nonlinear MHD ODEs backwards to the meeting point x_m to obtain another pair of $\{v, \alpha\}$. In other words, every value of x_s corresponds to a pair of $\{v, \alpha\}$. For a sequence of x_s values, another curve in the phase diagram is thus produced. The intersection points

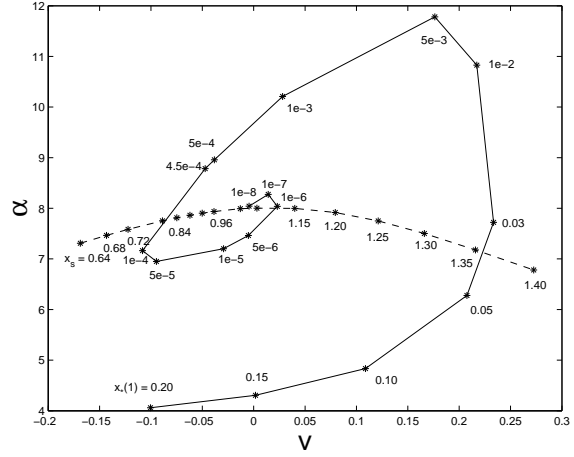


Figure 9. The phase diagram of Class I similarity MHD shock solutions with $\lambda = 0.1$. The meeting point is chosen at $x_m = 0.5$. The type 2 MHD eigensolution is used at the point $x_*(1)$ to integrate towards the meeting point. In the range of $x > x_s$, the magnetostatic SIS envelope with $A = 2$ and $V = 0$ is used to get this diagram. The values of $x_*(1)$ and x_s of the first three intersection points are $[x_*(1) = 0.0369, x_s = 1.3599]$, $[x_*(1) = 2.044 \times 10^{-4}, x_s = 0.7807]$ and $[x_*(1) = 1.10 \times 10^{-4}, x_s = 1.1266]$, respectively.

of the two phase curves represent matches of this type of similarity MHD shock solutions.

In Fig. 9, we show the relevant phase diagram of v and α following the matching procedure described above for a chosen meeting point at $x_m = 0.5$. Relevant parameters of the first three intersection points in the phase diagram are $(x_*(1), x_s) = (0.0369, 1.3599)$, $(2.044 \times 10^{-4}, 0.7807)$, $(1.10 \times 10^{-4}, 1.1266)$, respectively. In Figs. 10 and 11, we display the first three global MHD shock solutions of this type. Enlarged portions of these solutions are given in Fig 12.

When it comes to the Class II MHD shock solutions that connect downstream MHD LP solutions with a magnetostatic SIS envelope, the method of finding the solutions is similar to those described above. The key difference is that the downstream is now replaced by the MHD LP type solutions. In parallel, we could obtain similar phase diagram to identify the intersection points of phase curves. In Fig. 13, we present a relevant phase diagram of v and α to match similarity MHD shock solutions. In Fig. 14 and Fig. 15, we display the first three global MHD shock solutions of this type.

In Table 2, we summarize the properties of Class I and Class II MHD shock solutions matched with a magnetostatic SIS envelope, i.e., MEWCS solutions.

4.3 Similarity MHD Shock Breezes

MHD extensions for shock solutions of Shu et al. (2002) described in previous section should be viewed as a subset of Class II type MHD shock solutions. We now consider Class I type MHD shock solutions and allow the mass parameter A to vary (i.e., A cannot be equal to 2 in general) for a given x_* corresponding to a specific reduced central mass accretion rate m_0 . Both parameters A and x_s are adjusted gradually to match the upstream and downstream solutions in the

Table 2. Semi-complete Class I and II similarity MHD shock solutions matched with a magnetostatic SIS envelope.

Description	m_0	x_s	v_d	α_d	v_u	α_u	N
$x_*(1) = 0.0369$	0.0726	1.3599	0.4421	1.6024	0	1.0815	1
$x_*(1) = 2.044 \times 10^{-4}$	4.09×10^{-4}	0.7807	-0.2450	2.6333	-0.3428	2.4019	2
$x_*(1) = 1.10 \times 10^{-6}$	2.20×10^{-6}	1.1266	0.0567	1.6593	0	1.5758	3
$D = 11.26$	-	1.41944	0.5318	1.5847	0	0.9926	0
$D = 2156$	-	0.77598	-0.2478	2.6593	-0.3501	2.4177	1
$D = 4.04 \times 10^5$	-	1.12668	0.0569	1.6593	0	1.5755	2

Columns 1 to 8 provide relevant parameters for MHD shock solutions: $x_*(1)$ is the inner magnetosonic critical point for Class I MHD solutions and D is the central ‘density parameter’ of MHD LP type asymptotic solution for constructing Class II MHD solutions; m_0 is the reduced central mass accretion rate; x_s corresponds to both the shock location or shock speed; v_d is the downstream reduced speed; α_d is the downstream reduced density; v_u is the upstream reduced speed; α_u is the upstream reduced density and the number of stagnation points N indicates the number of nodes for sub-magnetosonic self-similar oscillations in MHD shock solutions.

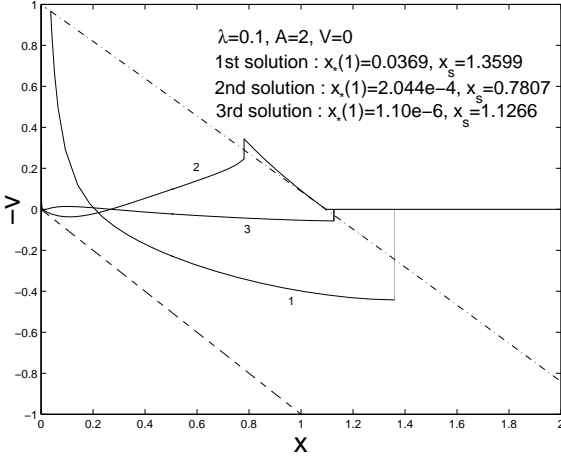


Figure 10. The first three Class I MHD shock solutions with $\lambda = 0.1$. The MHD shock solution 2 is an accretion MHD shock. The reduced radial speeds of the preshock and postshock are both negative. This similarity accretion MHD shock expands at a constant sub-magnetosonic speed. The type 2 MHD eigensolution is chosen at the point $x_*(1)$ to integrate towards the meeting point. In the range of $x > x_s$, the magnetostatic SIS envelope with $A = 2$ and $V = 0$ is used to get this diagram. The dash-dotted curve represents the magnetosonic critical curve. The dashed line is $x - v = 0$. The corresponding speed ratio v_A/a is shown in Fig. 11.

phase diagram of v versus α . We integrate from a specified x_* along the magnetosonic curve (in our calculations, we choose $x_* = 0.0369, 0.103, 0.2, 0.4, 0.7$ as several examples of illustration) with a type 2 MHD eigensolution towards the shock front at x_s to obtain the two parameters v_d and α_d . By the isothermal MHD shock conditions, we determine v_u and α_u for a given pair of v_d and α_d . Starting from v_u and α_u at x_s , we then integrate further the coupled nonlinear MHD ODEs to a chosen meeting point $x_m = 3.0$. Here, we apply the analytical asymptotic MHD solution (i) as given by equations (13) – (15) at $x = 20$ as the far-away ‘boundary condition’ to integrate backwards to $x_m = 3.0$. For a given x_* value and two series of x_s and A values, we then

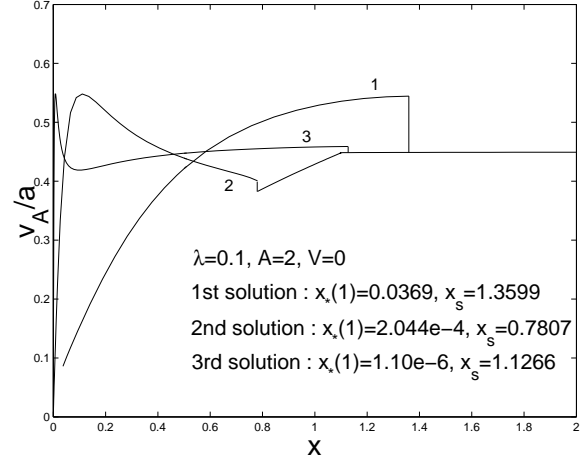


Figure 11. Corresponding to the shock solutions in Fig. 10, the ratio of the Alfvén wave speed to the isothermal sound speed v_A/a versus x with $\lambda = 0.1$. The first three Class I MHD shock solutions identified in the $\alpha - v$ phase diagram of Fig. 9. The type 2 MHD eigensolution is taken at the point $x_*(1)$ to integrate towards the meeting point. In the range of $x > x_s$, the magnetostatic SIS envelope with $A = 2$ and $V = 0$ is used for these MHD shocks.

draw a relevant phase diagram to determine the intersection point of the two phase curves, i.e., x_s and A . We could then construct such a similarity MHD shock breeze using the values of x_s and A at the intersection point. In Fig. 16, we display a sample phase diagram for the case of $x_* = 0.2$. For $x_* = 0.0369, 0.103, 0.4, 0.7$ respectively, we can obtain qualitatively similar phase diagrams (not shown here to avoid redundancy) and their corresponding x_s and A values. In Fig. 17, we present Class I isothermal MHD shock breeze solutions. The corresponding ratios of the Alfvén wave speed v_A to the isothermal sound speed a are shown in Fig 18. Table 3 contains the major relevant parameters for the shock solution examples of illustration.

Methods of determining Class II solutions of MHD shock breeze are similar to the above procedure. The main difference is to adopt the MHD LP type solutions for the

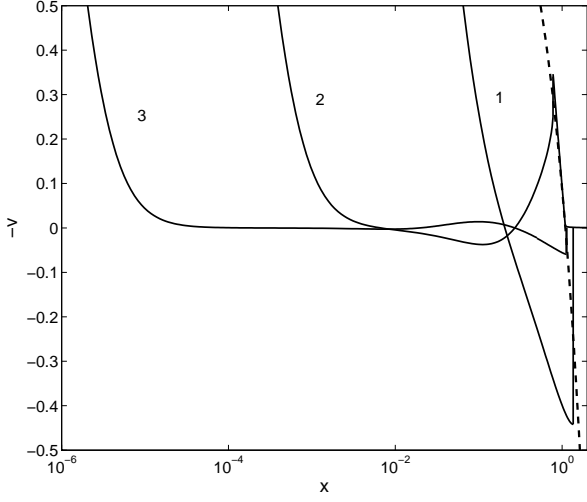


Figure 12. Enlarged portions of Class I MHD shock solution curves near $x \rightarrow 0^+$ of Fig. 10, emphasizing the diverging and oscillatory behaviours of this family of MHD shock solutions as $x \rightarrow 0^+$. The x -axis is shown in the logarithmic scale. The dashed line on the right is the magnetosonic critical curve. The undulatory profiles of the curves marked by numerals 1, 2, 3 represent self-similar sub-magnetosonic radial oscillations with one, two, three stagnation points, respectively.

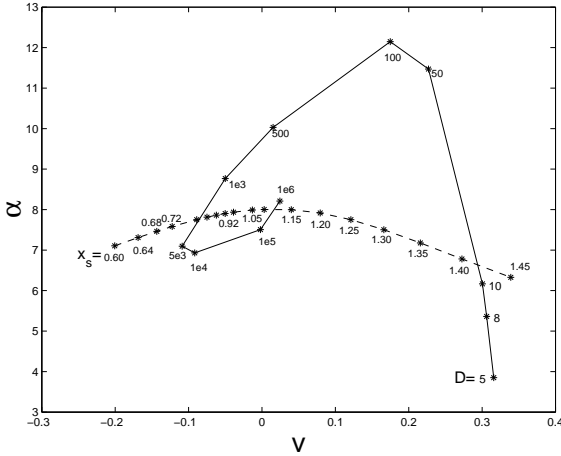


Figure 13. The phase diagram of Class II similarity MHD shock solutions with $\lambda = 0.1$. The meeting point is chosen at $x_m = 0.5$. The MHD LP type solution is used at the point near origin to integrate outward to the meeting point. In the range of $x > x_s$, the magnetostatic SIS envelope with $A = 2$ and $V = 0$ is specified for this diagram. The values of x_s and D of the first three intersection points are $(x_s = 1.41944, D = 11.26)$, $(x_s = 0.77598, D = 2156)$ and $(x_s = 1.12668, D = 4.04 \times 10^5)$, respectively.

downstream. Results of Class II MHD shock solutions have been discussed already in subsection 4.1.2 and we shall not repeat here.

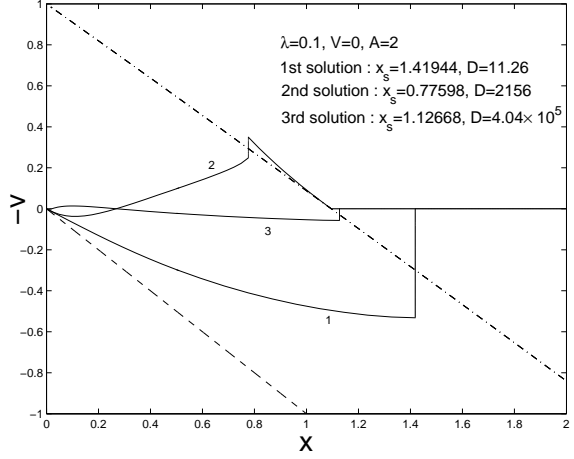


Figure 14. The first three class II MHD shock solutions with $\lambda = 0.1$ identified in the phase diagram of Fig. 13. The shock solution 2 is an accretion MHD shock with the reduced radial speeds of the preshock and postshock being both negative. This accretion MHD shock front expands at a constant sub-magnetosonic speed. The LP type MHD solution is used at near the origin to integrate outward to the meeting point. In the range of $x > x_s$, the magnetostatic SIS envelope with $A = 2$ and $V = 0$ is specified for this diagram. The dash-dotted line represents the magnetosonic critical curve and the straight dashed line represents the demarcation line of $x - v = 0$ for a positive enclosed mass. The speed ratio of the Alfvén wave speed to the isothermal sound speed v_A/a versus x is shown in Fig. 15.

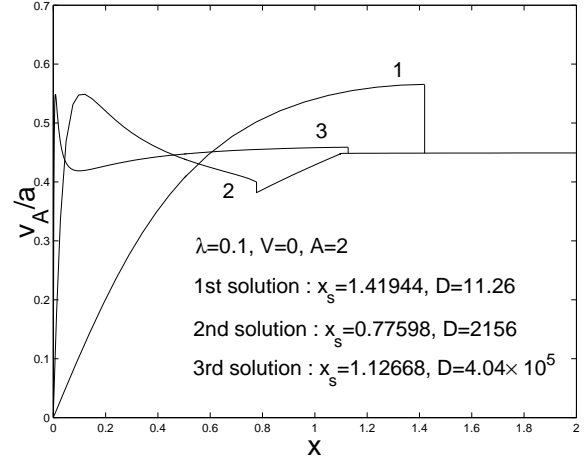


Figure 15. For the first three Class II MHD shock solutions with $\lambda = 0.1$ identified in the phase diagram of Fig. 13 and shown in Fig. 14, the corresponding ratio of the Alfvén wave speed to the isothermal sound speed v_A/a versus x is in display here. The MHD LP type solution is used near the origin to integrate outward to the meeting point. In the range of $x > x_s$, the magnetostatic SIS envelope with $A = 2$ and $V = 0$ is specified for this diagram.

4.4 Self-Similar Twin MHD Shock Solutions

In parallel with the investigation of Bian & Lou (2005), we can also construct twin shock solutions in the presence of a random magnetic field. All MHD shock solutions shown so far contain just a single MHD shock. In this subsection,

Table 3. Semi-complete Class I similarity MHD shock solutions matched with an asymptotic MHD breeze.

x_*	m_0	A	x_s	v_d	α_d	v_u	α_u
$x_* = 0.0369$	0.0724	2	1.3599	0.4414	1.6020	0	1.0828
$x_* = 0.103$	0.1952	1.8530	1.5018	0.5805	1.2907	0.1507	0.8802
$x_* = 0.2$	0.3586	1.8064	1.5146	0.5718	1.2050	0.2020	0.8655
$x_* = 0.4$	0.6356	1.8514	1.4216	0.4265	1.2520	0.1870	1.0091
$x_* = 0.7$	0.9107	1.9484	1.2492	0.1897	1.4401	0.1014	1.3294

Columns 1 to 8 provide the relevant parameters for MHD shock solutions: x_* is the magnetosonic critical point for Class I MHD shock breeze solutions; m_0 corresponds to the reduced central mass accretion rate; A is the mass density parameter of the upstream; the shock location is at x_s ; v_d is the downstream reduced velocity; α_d is the downstream reduced density; v_u is the upstream reduced velocity; and α_u is the upstream reduced density.

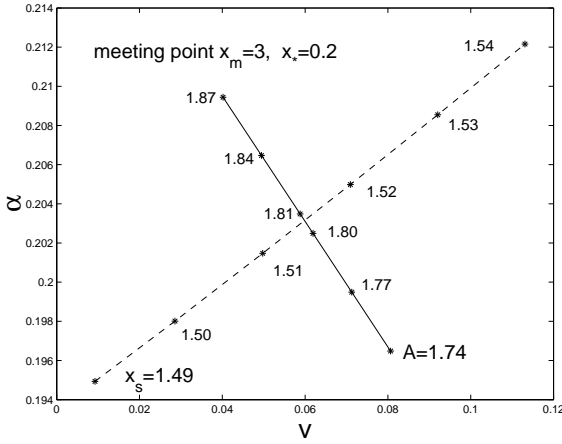


Figure 16. An example of illustration for the phase diagram of Class I MHD shock breeze solution with $\lambda = 0.1$ for the case of $x_* = 0.2$. For other values of x_* , similar phase diagrams are necessary to identify the relevant global MHD shock solutions. The type 2 MHD eigensolution is specified at the point $x_*(1)$ to integrate towards the meeting point. Analytical asymptotic MHD solution (i) as given by equations (13) – (15) with $V = 0$ and a varying A parameter is specified to integrate also towards the meeting point.

we are going to explore examples of semi-complete similarity solutions with twin MHD shocks. The upstream between the outer MHD shock and the magnetostatic state are tangent to the magnetosonic critical curve at the point of $x_*(2) = (1 + 2\lambda)^{1/2}$, which actually is part of MEWCS (Yu & Lou 2005). We may shift the location $x_*(2)$ somewhat towards the origin into the region of $0 < x < (1 + 2\lambda)^{1/2}$ and the upstream solution of the inner MHD shock may cross the magnetosonic critical curve analytically with a type 2 MHD eigensolution. We can subsequently construct Class I and Class II twin MHD shock solutions in the $\alpha - v$ phase diagram. For constructing Class I twin MHD shock solutions, we first specify the value of $x_*(2)$ and adjust the value of $x_*(1)$ point and the shock location $x_s(1)$ between $x_*(1)$ and $x_*(2)$ to search for similarity MHD shock solution crossing the magnetosonic critical curve analytically using the intersections of phase curves in the $\alpha - v$ phase diagram. More specifically, we choose a meeting point $x_m = 0.5$ and integrate an upstream solution of the inner shock from $x_*(2)$

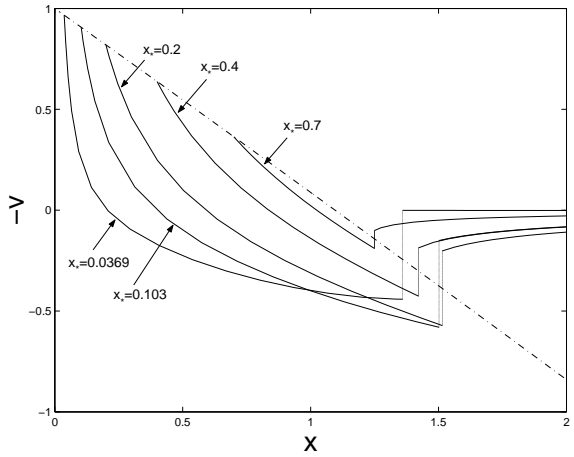


Figure 17. The Class I MHD shock solutions with $\lambda = 0.1$. The type 2 MHD eigensolution is specified at the point $x_*(1)$ along the magnetosonic critical curve to integrate towards the meeting point x_m . Analytical asymptotic MHD solution (i) as given by equations (13) – (15) with $V = 0$ and a varying A parameter is invoked to also integrate towards the meeting point x_m . The dash-dotted line represents the magnetosonic critical curve. The speed ratio of v_A/a is shown in Fig. 18.

for Class I solutions using a type 2 MHD eigensolution as initial conditions to a chosen shock location $x_s(1)$ in order to get the upstream values of v_u and α_u at the inner shock location $x_s(1)$. We next use the isothermal MHD shock conditions to determine the downstream values of v_d and α_d at the inner shock location $x_s(1)$. We then integrate from v_d and α_d at $x_s(1)$ towards the meeting point $x_m = 0.5$. Meanwhile, we also integrate forward from $x_*(1)$ again using type 2 MHD eigensolution to $x_m = 0.5$. In Fig. 19, we show the phase diagram of Class I MHD shock solution for two cases $x_*(2) = 0.9$ and 1.0 , respectively (n.b., phase curves of Class II MHD shock solution are also included in this figure). From the intersections of phase curves, we obtain the relevant parameter pair $[x_*(1), x_s(1)]$ of Class I MHD shock solutions as $(1.44 \times 10^{-4}, 0.8352)$ for the case of $x_*(2) = 0.9$ and as $(1.88 \times 10^{-4}, 0.7901)$ for the case of $x_*(2) = 1.0$. We show the corresponding Class I MHD shock solutions for $-v$ versus x in Fig. 20 as an example of illustration. In Fig. 21, we

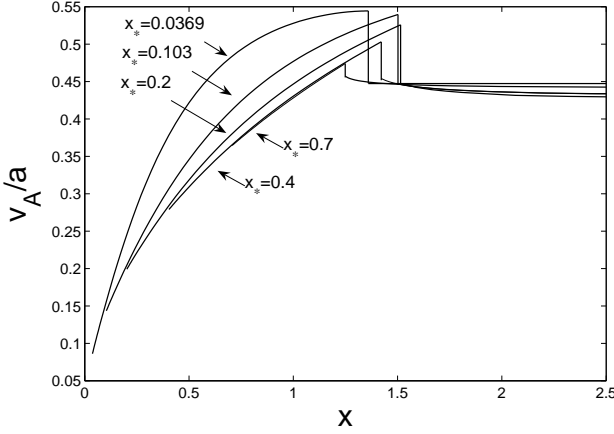


Figure 18. The ratios of the Alfvén wave speed and the isothermal sound speed v_A/a with $\lambda = 0.1$ corresponding to the MHD shock breeze results in Fig. 17.

show the corresponding ratios of the Alfvén wave speed v_A to the isothermal sound speed a .

For constructing Class II twin MHD shock solutions, we first specify the value of x_* and adjust the value of central reduced mass density D parameter together with the MHD shock location $x_s(1)$ between 0 and x_* to search for similarity MHD shock solutions using the intersections of phase curves in the $\alpha - v$ phase diagram. From the intersections of phase curves in Fig. 19, we identify the relevant parameter pair $[D, x_s(1)]$ of Class II MHD shock solutions as (3059, 0.8297) for the case of $x_* = 0.9$ and as (2344, 0.7854) for the case of $x_* = 1.0$. We present the corresponding Class II MHD shock solutions for $-v$ versus x in Fig. 22 as another example of illustration. The corresponding ratios of the Alfvén wave speed v_A to the isothermal sound speed a are shown in Fig 23.

In Fig. 19, relevant phase curves of both Class I and Class II twin MHD shock solutions are presented, where the meeting point $x_m = 0.5$ is chosen. In this phase diagram, both cases of $x_*(2) = 0.9$ and $x_*(2) = 1.0$ for Class I solution and of $x_* = 0.9$ and $x_* = 1.0$ for Class II solution are plotted. Using the intersection points of phase curves in this phase diagram, we can readily construct the inner Class I and Class II MHD shock solutions, respectively.

The above procedures are implemented to search for the inner MHD shock solutions. In the range of $x > x_*(2)$ for Class I solution (or $x > x_*$ for Class II solution), we can further construct the outer MHD shock by choosing different outer shock location $x_s(2)$. For $x_*(2) = 0.9$ (for Class I) or $x_* = 0.9$ (for Class II), we choose $x_s(2) = 0.95, 1.00, 1.10, 1.15, 1.20, 1.25$, respectively, while for $x_*(2) = 1.0$ (for Class I) or $x_* = 1.0$ (for Class II), we choose $x_s(2) = 1.05, 1.10, 1.15$, respectively. The upstream asymptotic MHD solutions across the outer shock can match with the analytical asymptotic solution (13) – (15) for $x \rightarrow +\infty$. When the value of the outer shock location $x_s(2)$ is smaller, the upstream would be an MHD inflow (contraction or accretion). As the value of MHD shock location $x_s(2)$ increases, the upstream would become an MHD outflow (expansion or wind or breeze). Relevant solutions are displayed in Fig. 24–Fig. 27

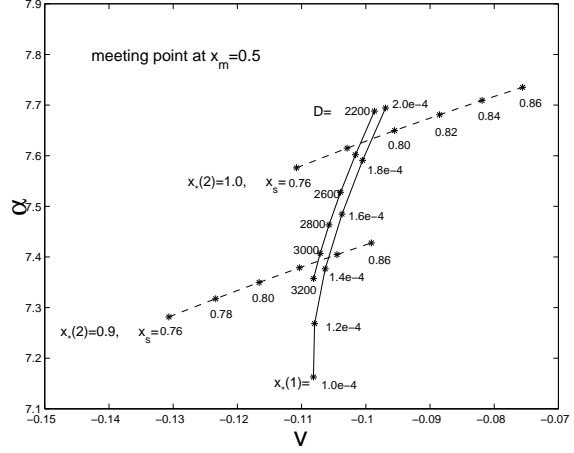


Figure 19. A phase diagram of v versus α at a chosen meeting point $x_m = 0.5$ for constructing MHD shock solutions with $\lambda = 0.1$. In this phase diagram, both cases of $x_*(2) = 0.9$ and $x_*(2) = 1.0$ for Class I MHD shock solutions and of $x_* = 0.9$ and $x_* = 1.0$ for Class II MHD shock solutions are shown.

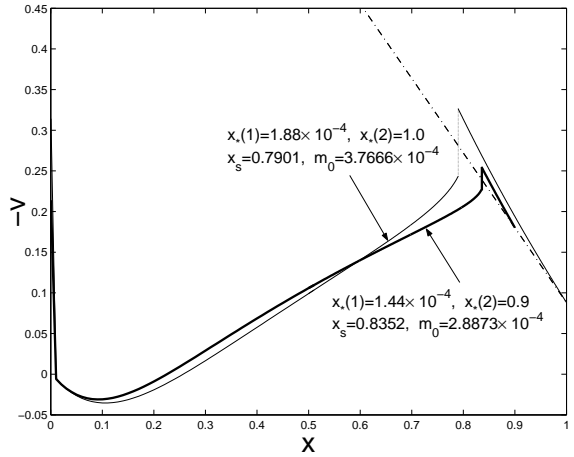


Figure 20. Class I MHD shock solutions with $\lambda = 0.1$ for $x_*(2) = 0.9$ and 1.0 shown in terms of $-v(x)$ versus x by the heavy and light solid curves, respectively. The two corresponding values of inner magnetosonic point $x_*(1)$ are 1.44×10^{-4} and 1.88×10^{-4} , respectively. The two corresponding inner MHD shocks are located at $x_s = 0.8352$ and $x_s = 0.7901$, respectively. The dash-dotted line represents the magnetosonic critical curve. The speed ratio v_A/a versus x is shown in Fig. 21.

4.5 Novel Class III MHD Shock Solutions

In our numerical investigation, we also construct a unique Class III solutions exclusive to MHD shock solutions. This type of solutions carry a mixed feature of both Class I and Class II solutions. Their reduced velocity is a finite convergent inflow, similar to Class II solutions towards the centre. Their reduced mass density is divergent, characteristic of Class I solutions towards the centre. Starting from equations (22) and (23), we can construct these new Class III MHD solutions. In order to assure the existence of this Class III solutions, λ should be greater than 4 (Wang & Lou 2006). As examples of illustration, we take $K = 1.0$, $\lambda = 5.0$, $H = [2 - \lambda + (\lambda^2 - 4\lambda)^{1/2}]/2$ and $x_s = 1.2, 1.5, 1.7, 2.2$,

Table 4. Semi-complete Class I and II similarity twin MHD shock solutions matched with different outer magnetosonic critical point $x_*(2)$.

$x_*(2)$	Description	$x_s(1)$	$x_s(2)$	A	V
0.90	$x_*(1) = 1.44 \times 10^{-4}$ $m_0 = 2.8873 \times 10^{-4}$ $D = 3059$	0.8352	0.95	1.5552	-0.3852
			1.00	1.6398	-0.3034
		0.8297	1.10	1.8546	-0.1103
			1.15	1.9868	0
			1.20	2.1401	0.1198
			1.25	2.3238	0.2553
1.00	$x_*(1) = 1.88 \times 10^{-4}$ $m_0 = 3.7666 \times 10^{-4}$ $D = 2344$	0.7901	1.05	1.8414	-0.1298
			1.10	1.9615	-0.0289
		0.7854	1.15	2.1070	0.0869

Columns 1 to 6 give the values of $x_*(2)$ where the Class I and Class II twin shock solutions cross the sonic critical line the second time, $x_*(1)$ and m_0 for Class I solutions, D for Class II solutions, the first shock location $x_s(1)$, the second shock location $x_s(2)$, the mass density parameter A and the speed parameter V .

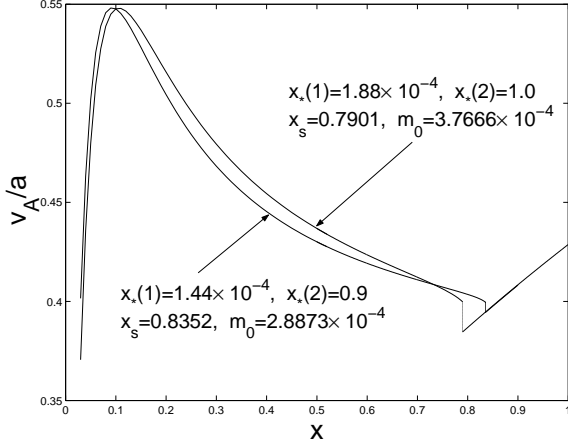


Figure 21. Class I MHD shock solutions with $\lambda = 0.1$ for $x_*(2) = 0.9$ and 1.0 for the ratio of the Alfvén wave speed and the isothermal sound speed v_A/a versus x for the solutions shown in Fig. 20. The two corresponding values of $x_*(1)$ are 1.44×10^{-4} and 1.88×10^{-4} , respectively. The corresponding inner MHD shock is located at $x_s = 0.8352$ and $x_s = 0.7901$, respectively.

respectively. In Figs. 28 and 29, we present these Class III MHD shock solutions.

4.6 Two-Temperature Similarity MHD Shocks

We have only studied so far the case of $\tau = 1$ in the preceding sections. This means that both the downstream and upstream magnetofluids across an MHD shock have the same thermal temperature, i.e., the entire magnetofluid has same thermal sound speed $a_u = a_d$. In some astrophysical systems (e.g., HII regions around luminous massive OB stars), the factor of determining the ionization temperature, mean atomic mass, etc., would vary from an interior region to an exterior region. In this section, we shall discuss a magnetized gas medium of two different temperatures across an MHD shock. In our following consideration, the downstream sound speed a_d is thus no longer equal to the upstream sound speed

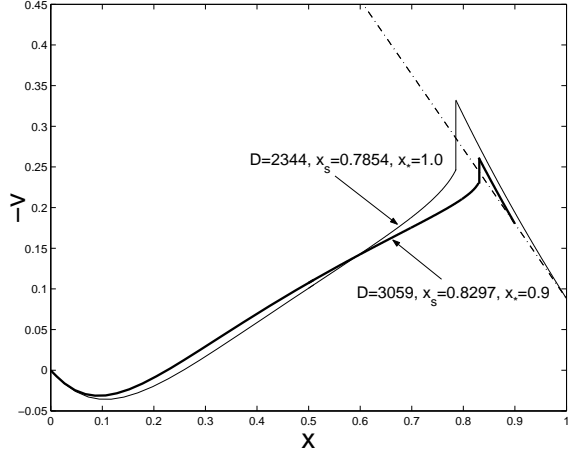


Figure 22. Class II MHD shock solutions with $\lambda = 0.1$ for $x_* = 0.9$ and 1.0 in terms of $-v(x)$ versus x by the heavy and light solid curves, respectively. The corresponding values of (D, x_s) are $(3059, 0.8297)$ and $(2344, 0.7854)$, respectively. The dash-dotted line represents the magnetosonic critical curve. The speed ratio v_A/a versus x is shown in Fig. 23.

a_u . In most astrophysical systems, the downstream sound speed should be faster than the upstream sound speed, while the downstream and upstream fluids can be regarded as isothermal fluids separately. With this in mind, we assume $a_d/a_u > 1$ in our following MHD model analysis.

Let us begin with the MHD shock solution for the case of $V = 0$ at $x \rightarrow +\infty$. Here, we take Class I MHD solutions with a magnetosonic critical point $x_*(1) = 0.103$ and Class II MHD solutions with a central reduced density parameter $D = 0.1$ as examples of illustration. For different values of sound speed ratio a_d/a_u , we obtain the Class I and Class II MHD shock solutions through matching the upstream and downstream solutions in the speed-density phase diagram.

In Fig. 30 and Fig. 31, we display both classes of MHD shock solutions with their parameters summarized in Table 5. In both classes of MHD shock solutions, as the ratio a_d/a_u

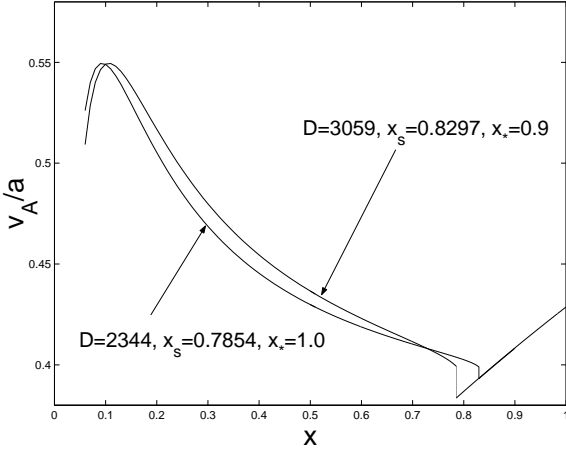


Figure 23. Class II MHD shock solutions with $\lambda = 0.1$ for $x_* = 0.9$ and 1.0 shown for the ratio of the Alfvén wave speed to the isothermal sound speed v_A/a versus x corresponding to the results of Fig. 22. The corresponding values of (D, x_s) are $(3059, 0.8297)$ and $(2344, 0.7854)$, respectively.

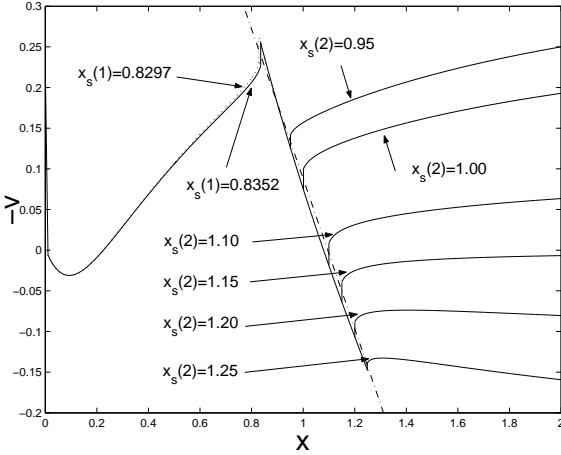


Figure 24. Class I (solid curve) and Class II (dotted curve) twin MHD shock solutions with $\lambda = 0.1$ for $x_* = 0.9$ are shown in terms of $-v(x)$ versus x . The dash-dotted line represents the magnetosonic critical curve. The outer MHD shock locations $x_s(2)$ are located at 0.95, 1.00, 1.10, 1.15, 1.20, 1.25 to match with various asymptotic MHD solutions at $x \rightarrow +\infty$. The corresponding speed ratios v_A/a versus x are shown in Fig. 25.

increases, the downstream shock location x_{sd} , namely, the Mach number of the downstream shock becomes smaller. The mass parameter A increases with an increasing a_d/a_u ratio. When the mass parameter A is less than 2, the upstream solution is an MHD outflow breeze. The MHD breeze is stronger with a smaller value of A . In the case of the mass parameter A larger than 2, the inflow speed becomes weaker when A becomes smaller.

We now investigate the case for the velocity parameter $V \neq 0$. For instance, we choose $a_d/a_u = 1.5$ to study Class II MHD shock solutions. Different locations of x_{sd} lead to different MHD shock solutions. In Fig. 32 and Fig. 33, we

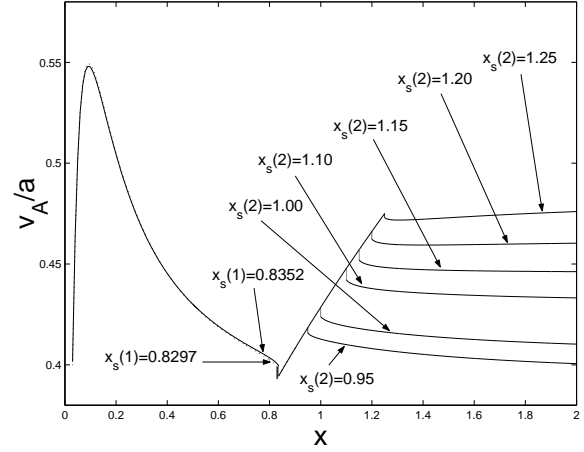


Figure 25. Class I (solid curve) and Class II (dotted curve) twin MHD shock solutions with $\lambda = 0.1$ for $x_* = 0.9$ are shown in terms of the ratio of the Alfvén wave speed to the isothermal sound speed v_A/a versus x corresponding to results of Fig. 24. The outer MHD shocks locations $x_s(2)$ are at 0.95, 1.00, 1.10, 1.15, 1.20, 1.25 respectively to match with various asymptotic MHD solutions at $x \rightarrow +\infty$.

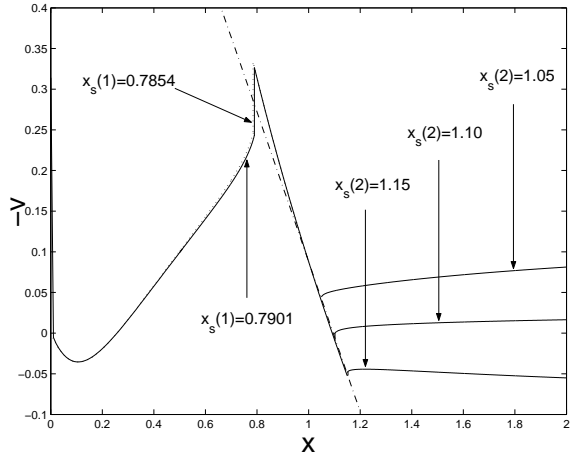


Figure 26. Class I (solid curve) and Class II (dotted curve) twin MHD shock solutions with $\lambda = 0.1$ and the magnetosonic point $x_* = 1.0$ shown in terms of $-v(x)$ versus x . The dash-dotted line represents the magnetosonic critical curve. The outer MHD shock locations $x_s(2)$ are at 1.05, 1.10, 1.15, respectively to match with various asymptotic MHD solutions at $x \rightarrow +\infty$. The corresponding speed ratio v_A/a versus x is shown in Fig. 27.

present different MHD shock solutions with the reduced central density parameter $D = 10^{-6}$.

5 NOTES AND DISCUSSION

In this paper, we investigated quasi-spherical self-similar shock solutions for magnetized self-gravitating isothermal fluids in the semi-complete solution space. The relevant similarity MHD shock solutions are obtained and classified by comparing with results of previous analyses (Tsai & Hsu 1995; Shu et al. 2002; Lou & Shen 2004; Shen & Lou 2004;

Table 5. Two-temperature Class I and II similarity MHD shock breeze solutions with different values of sound speed ratio a_d/a_u .

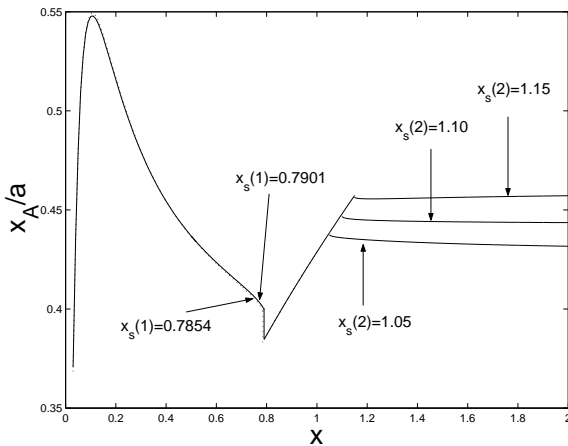
Parameter	a_d/a_u	A	x_{sd}	x_{su}	v_d	α_d	v_u	α_u
$x_*(1) = 0.103$	1	1.8530	1.5018	1.5018	0.5805	1.2907	0.1507	0.8802
	1.3	2.7594	1.4834	1.9284	0.5750	1.3150	-0.4102	0.6640
	1.5	3.5226	1.4612	2.1918	0.5682	1.3452	-0.6657	0.6305
	1.8	4.9048	1.4414	2.5945	0.5622	1.3729	-0.9916	0.6059
$D = 0.1$	1	0.2976	2.3960	2.3960	1.7176	0.1563	0.8273	0.0676
	1.3	0.4226	2.3120	3.0056	1.6517	0.1521	0.5082	0.0523
	1.5	0.5288	2.2786	3.4179	1.6256	0.1505	0.3913	0.0487
	1.8	0.7206	2.2480	4.0464	1.6018	0.1491	0.2675	0.0459

Columns 1 to 9 contains relevant parameters of MHD shock solutions: $x_*(1)$ for the magnetosonic critical point of Class I MHD solutions and D for the central reduced density parameter of Class II MHD solutions; the sound speed ratio of the downstream a_d to the upstream a_u ; the upstream mass density parameter A ; x_{sd} is the shock location in terms of downstream a_d ; x_{su} is the shock location in terms of upstream a_u ; the downstream reduced speed v_d ; the downstream reduced density α_d ; the upstream reduced speed v_u ; the upstream reduced density α_u .

Table 6. Two-temperature Class II MHD shock solutions for sound speed ratio $a_d/a_u = 1.5$ with $D = 10^{-6}$.

x_{sd}	x_{su}	v_d	α_d	v_u	α_u	A	V
2.0	3.00	1.4407	1.5753×10^{-6}	-0.2092	4.1184×10^{-7}	3.3637×10^{-6}	-0.7544
2.5	3.75	1.8608	2.0284×10^{-6}	0.7814	6.5518×10^{-7}	8.3927×10^{-6}	0.2820
3.0	4.50	2.3032	2.7282×10^{-6}	1.6533	1.0016×10^{-6}	1.8592×10^{-5}	1.1984

Columns 1 to 8 summarize relevant parameters for MHD shock solutions. x_{sd} is the shock location in terms of downstream a_d ; x_{su} is the shock location in terms of upstream a_u ; the downstream reduced velocity is v_d ; the downstream reduced density is α_d ; the upstream reduced velocity is v_u ; the upstream reduced density is α_u ; A is for the mass density parameter of upstream and V is the upstream speed parameter.


Figure 27. Class I (solid curve) and Class II (dotted curve) twin MHD shock solutions with $\lambda = 0.1$ and a magnetosonic critical point $x_* = 1.0$ shown in terms of the speed ratio v_A/a versus x corresponding to the MHD shock results of Fig. 26. The outer MHD shock locations $x_s(2)$ are at 1.05, 1.10, 1.15, respectively, to match with various asymptotic MHD solutions at $x \rightarrow +\infty$.

Bian & Lou 2005; Yu & Lou 2005). For a closely relevant similarity analysis on a magnetized polytropic gas, the reader is referred to Wang & Lou (2006). Such mEECC sim-

ilarity solutions, which depict an expanding envelope with a concurrent collapsing core, are derived from nonlinear MHD equations and may be applied to various astrophysical MHD processes with appropriate adaptations.

As noted by Yu & Lou (2005), the velocity and density profiles of an EECC shock model agree better with observations of cloud B335 than the results of the EWCS model. The magnetized EECC shock solutions qualitatively retain this essential feature of nonmagnetized EECC solutions (Shen & Lou 2004). The inclusion of a random magnetic field is more realistic and can be further utilized to model diagnostic features such as synchrotron emissions etc. Due to current observational limits, no empirical magnetic field information is immediately available for the most inner core of cloud system B335 (e.g., Wolf et al. 2003). Our MHD EECC shock solutions may give a rough estimate for the magnetic field strength in the most inner core of star forming cloud B335 as an example. For the starless cloud system B335, we may take an infalling region of a spatial scale $\sim 1.5 \times 10^4$ AU, a cloud mass of $\sim 4M_\odot$, a random magnetic field strength of $\sim 134\mu\text{G}$ (e.g., Wolf et al. 2003) and a thermal sound speed $a \sim 0.23 \text{ km s}^{-1}$. For a quasi-spherical accretion MHD shock to exist within such a cloud system, the core magnetic field strength may reach $\sim 1\text{mG}$, which is several times strong than our previous estimate of $\sim 300\mu\text{G}$, depending on the strength of such an MHD

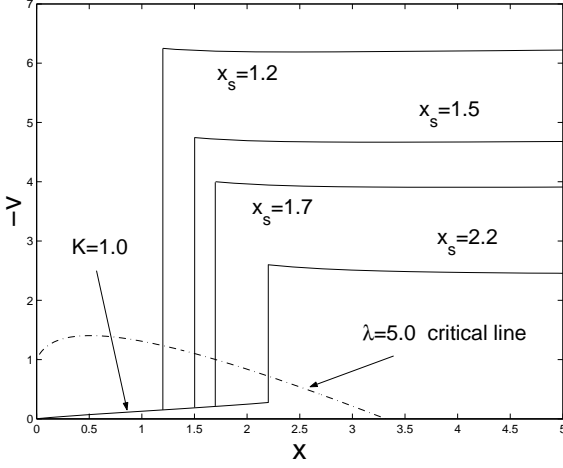


Figure 28. Semi-complete Class III MHD shock solutions in terms of $-v(x)$ versus x with $\lambda = 5.0$ and $K = 1.0$ for shock location $x_s = 1.2, 1.5, 1.7, 2.2$, respectively. Asymptotic MHD solutions (iv) given by equations (22) and (23) are specified near the origin. The dash-dotted line represents the magnetosonic critical curve. The speed ratio v_A/a versus x is shown in Fig. 29.

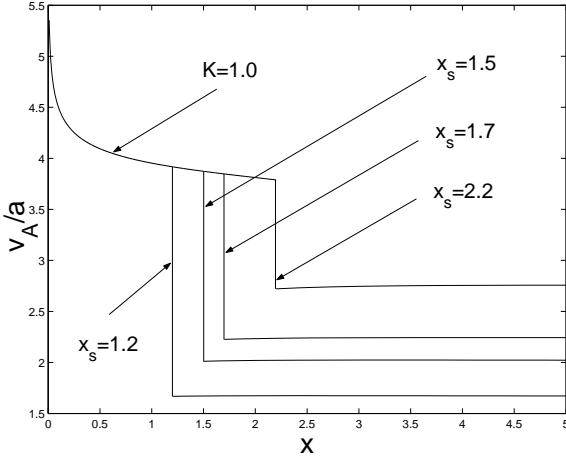


Figure 29. The ratio of the Alfvén speed to the isothermal sound speed v_A/a versus x with $\lambda = 5.0$ and $K = 1.0$, corresponding to the MHD shock results in Fig. 28. Class III MHD shock solutions with the MHD shock location at $x_s = 1.2, 1.5, 1.7, 2.2$, respectively.

shock. Observations indicate that some T Tauri stars may have surface magnetic field strengths of the order of 10^3 G, which is much greater than our estimate. Possibly, our quasi-spherical solutions may not be valid when the spatial scale involved becomes much smaller than ~ 100 AU; within such a scale, a circumstellar disc as well as the stellar dynamo process would dominate among various processes to amplify the protostellar magnetic fields (n.b., a small-scale circumstellar disc and a relevant bipolar outflow would be regarded as additional features in our quasi-spherical mEECC shock scenario).

Such mEECC similarity solutions with a random magnetic field may also be applied to the asymptotic giant branch (AGB) phase or post-AGB phase in the late evolution stage of a low-mass main-sequence star before the

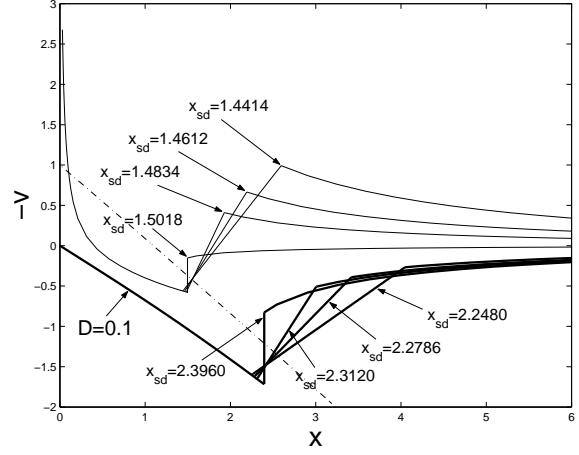


Figure 30. Class I (light solid curves) two-temperature MHD shock breeze solutions with $\lambda = 0.1$, $x_* = 0.103$ and different density ratio $\alpha_d/\alpha_u \geq 1$. Class II (heavy solid curves) two-temperature MHD shock breeze solutions with $\lambda = 0.1$, $D = 0.1$ and different density ratio $\alpha_d/\alpha_u \geq 1$. The dash-dotted line represents the magnetosonic critical curve. The reduced transverse magnetic field strength $b(x)$ versus x is shown in Fig. 31.

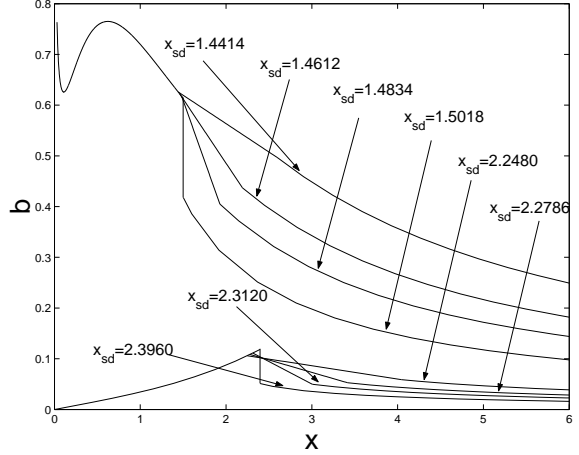


Figure 31. Reduced transverse magnetic field strength $b(x)$ versus x corresponding to the results in Fig. 30. Class I two-temperature MHD shock breeze solutions with $\lambda = 0.1$, $x_* = 0.103$ and different density ratio $\alpha_d/\alpha_u \geq 1$. Class II two-temperature MHD shock breeze solutions with $\lambda = 0.1$, $D = 0.1$ and different density ratio $\alpha_d/\alpha_u \geq 1$.

gradual emergence of a planetary nebula (PN) system with a central magnetized white dwarf of a high surface temperature in the range of $1 \times 10^5 \sim 2 \times 10^5$ K. The timescale of this evolution ‘gap’ between these two phases is estimated to be $\sim 10^3$ yrs. Planetary nebulae and proto-planetary nebulae (pPNs) are believed to be the ultimate evolutionary stages of low- and intermediate-mass stars ($M \leq 8M_\odot$). PNs and pPNs appear on the sky as expanding plasma clouds surrounding a luminous central star. Such expanding clouds have a typical asymptotic speed of $\sim 10 - 20$ km s $^{-1}$; the relevant mass loss rates fall within the range of $\sim 10^{-8}$ to $\sim 10^{-4} M_\odot$ yr $^{-1}$. With an insufficient nuclear fuel supply from a certain epoch on, the central region starts to contract and collapse while the outer envelope continues to expand

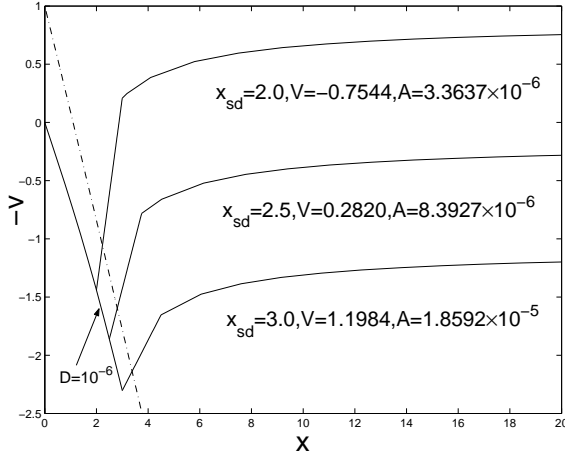


Figure 32. Class II MHD shock solutions with $\lambda = 0.1$ and $D = 10^{-6}$ shown in terms of $-v(x)$ versus x by light solid curves. The dash-dotted line represents the magnetosonic critical curve. The reduced transverse magnetic field $b(x)$ versus x is shown in Fig. 33.

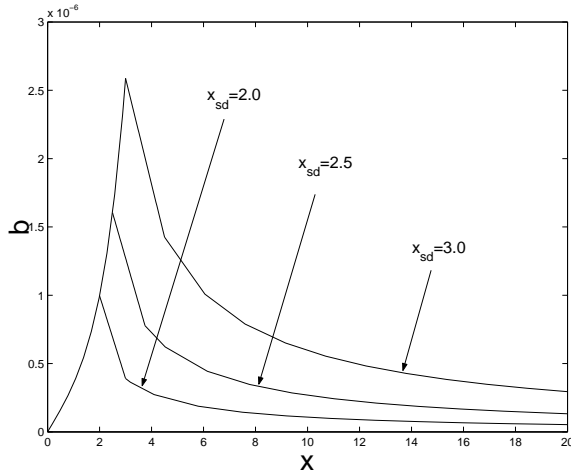


Figure 33. The reduced transverse magnetic field $b(x)$ versus x corresponding to the Class II MHD shock solutions with $\lambda = 0.1$ and $D = 10^{-6}$ shown in Fig. 32.

into a massive wind; it is highly likely that the central collapse is accompanied by an outward energetic surge to chase the slowly expanding envelope. Thus a slow, dense stellar wind expelled during the AGB phase is followed by a fast, tenuous magnetized wind driven off the collapsing proto-white dwarf during the PN phase. The collision of magnetized winds with two different flow speeds would inevitably generate an MHD shock. In this process, the outer expansion removes stellar envelope mass accompanied by a proto white dwarf produced at the centre by central infall and collapse. Sufficiently far away from the initial and boundary conditions, the system may gradually evolve into an MHD phase representable by an MHD EECC similarity solution during a timescale of a few hundred to several thousand years. As noted out by Bian & Lou (2005), the dimensionless mass accretion rate m_0 should be in the range of $\sim 10^{-3} - 10^{-4}$. In a PN, the dimensionless magnetic parameter λ is about 0.003. Our Class I twin MHD shock solutions appears to

have the desired reduced mass accretion rate towards the collapsed core.

Observations grossly indicate a magnetic field strength of $\sim 1\text{G}$ near the stellar surface at $r \sim 1\text{AU}$ during the AGB phase, decreasing approximately to $\sim 10^{-3}\text{G}$ at $r \sim 10^3\text{AU}$. In the quasi-spherical self-similar MHD expansion regime of our model analysis, the transverse magnetic field strength scales as $B_{\perp} \propto r^{-1}$ (e.g., Lou 1993, 1994); for an expanding MHD shock travelling outwards, the magnetic field downstream would be enhanced by the existence of such an MHD shock. Our model estimates are roughly consistent with the measured magnetic field variations observed for AGB stars. The magnetic field strength associated with an MHD EECC solution in the innermost collapse region scales as $B \propto r^{-1/2}$. If we take the strength of a surface magnetic field as $\sim 1\text{G}$ at $r \sim 1\text{AU}$ and the radius of a proto-white dwarf as $\sim 6000\text{ km}$, then the magnetic field strength estimated at the surface of a proto-white dwarf is roughly 10^3G . An accretion MHD shock would further increase this inner downstream magnetic field. This enhancement is determined by the MHD shock strength. Much stronger surface magnetic fields of a magnetic white dwarf ($\sim 10^6 - 10^9\text{G}$) might be generated and sustained by intrinsic stellar MHD dynamo processes driven by the convective differential rotation inside an AGB star (e.g., Blackman et al. 2001).

We therefore hypothesize that dynamical evolution of an mEECC phase of around or less than a few thousand years may be the missing linkage between the AGB or post-AGB phase and the gradual appearance of a PN. Depending on physical parameters of the low-mass progenitor star, it may also happen that the degenerate CO core collapse and subsequent material infalls during an mEECC phase lead to an eventual core mass exceeding the Chandrasekhar mass limit of $1.4M_{\odot}$ and thus induce a supernova with an intensity determined by the actual central mass accretion rate.

For the Crab Nebula as an example of magnetized SNR, we model the nebular magnetic field as $B_{\perp} \propto r^{-1}$ during the outer envelope expansion phase, ignoring complex interactions between the central magnetized relativistic pulsar wind and the inner nebula. In the presence of shocks, as a flow passes through a shock from downstream to upstream, the magnetic field strength would decrease by a factor of a few. Thus, the magnetic field strength in the flow would change in the presence of shocks as compared with mEECC solutions without shocks, although not significantly. For a neutron star of a radius $\sim 10\text{ km}$ and a typical dipolar magnetic field of strength $\sim 10^{10}\text{G}$ (we exclude for the moment those unusual high-field magnetars, such as SGRs and AXPs whose magnetic field strength may reach as high as $10^{14} \sim 10^{15}\text{G}$), the magnetic field would decrease to $\sim 10^{-3}\text{G}$ at a distance of about several parsecs (Yu & Lou 2005). When an MHD shock is included and for the same neutron star magnetic field, the outer nebular magnetic field would become weaker $\sim 10^{-4}\text{G}$ at a distance of about several parsecs. These estimates more or less agree with the magnetized envelope expansion portion of our mEECC shock solutions. In addition to this order of magnitude agreement with observations for magnetic field strengths, mysterious central structures of the Crab Nebula like wisps and knots are likely produced by reverse fast MHD shock waves as a result of slightly inhomogeneous pulsar wind streams emanating from the fast spinning pulsar (e.g., Lou 1998). These quasi-stationary re-

verse MHD shocks in space can effectively produce relativistic particles and synchrotron emissions from relativistic electrons gyrating rapidly around magnetic field lines surrounding these compact objects. The familiar triple ring structure of SN1987A may be associated with MHD shocks (Tanaka & Washimi 2002).

Unlike the Crab Nebula, which is primarily powered by the rotational energy through a relativistic pulsar wind, the slowly rotating magnetars are thought to be powered by the decay of extremely intense magnetic field. The light curves may thus represent an adiabatically expanding population of electrons accelerated at a particularly active phase, which could be produced by the ejecta colliding with a pre-existing shell. Such a shell is naturally made by SGR itself, because its quiescent wind of a luminosity $\sim 10^{34}$ erg s $^{-1}$ will sweep up a bow shock of a stand-off distance $\sim 10^{16}$ cm as it moves through the interstellar medium (ISM) at a typical neutron star velocity of ~ 200 km s $^{-1}$. If this pre-existing shell is hit by giant flares from a SGR with an energy of $\sim 10^{43} - 10^{44}$ erg, MHD shocks will naturally occur and be swept outward, resulting in a violent episode of relativistic particle acceleration that deposits much of the energy into a steadily expanding synchrotron-emitting shell after giant flares. Polarized emissions from SGRs also indicate that magnetic field should play a crucial role in understanding SGR phenomena.

As massive OB stars turn on their core nuclear reactions in magnetized molecular clouds, the interstellar medium of surrounding neutral hydrogen gas strongly absorbs ultraviolet radiations from OB stars and becomes ionized to form luminous HII regions (e.g., Strömgren 1939; Osterbrock 1989; Shu et al. 2002). As the ionization front sweeps through the neutral cloud, magnetized gas flows driven by pressure gradients develop between HII and HI regions as well as within HII regions, and MHD shocks can naturally emerge in these processes.

For astrophysical systems of much larger scales such as clusters of galaxies (e.g., Sarazin 1988; Fabian 1994), the similarity MHD shock solutions may be valuable for understanding a certain phase of their evolution involving magnetic fields (e.g., Hu & Lou 2004; Lou 2005). Chandra observations show that the continuous blowing of bubbles by the central radio source would lead to the propagation of shocks seen as the observed fronts and ripples, gives a rate of working which balances the radiative cooling within the cluster core (Fabian et al. 2003). With appropriate adaptation, our MHD shock model may offer interesting interpretations of such phenomena.

ACKNOWLEDGMENTS

This research has been supported in part by the ASCI Center for Astrophysical Thermonuclear Flashes at the University of Chicago under the Department of Energy contract B341495, by the Special Funds for Major State Basic Science Research Projects of China, by the Tsinghua Center for Astrophysics, by the Collaborative Research Fund from the National Science Foundation of China (NSFC) for Young Outstanding Overseas Chinese Scholars (NSFC 10028306) at the National Astronomical Observatories of China, Chinese Academy of Sciences, by the NSFC grants 10373009 and 10533020 at the Tsinghua University, and by the SRFDP

20050003088 and the Yangtze Endowment from the Ministry of Education at the Tsinghua University. Affiliated institutions of Y-QL share this contribution.

REFERENCES

- Adams F. C., Lada C. J., Shu F. H., 1987, *ApJ*, 321, 788
- Balick B., Frank A., 2002, *ARA&A*, 40, 439
- Barenblatt G. I., Zel'dovich Ya. B., 1972, *AnRfM*, 4, 285
- Bazer J., Ericson W. B., 1959, *ApJ*, 129, 758
- Bertschinger E., 1985, *ApJS*, 58, 39
- Bian F.-Y., Lou Y.-Q., 2005, *MNRAS*, 363, 1315
- Blackman E. G., Frank A., Markiel J. A., Thomas J. H., Van Horn H. M., 2001, *Nature*, 409, 485
- Blandford R. D., McKee C. F., 1976, *Physics of Fluids*, 19, 1130
- Blandford R. D., McKee C. F., 1977, *MNRAS*, 180, 343
- Blondin J. M., Chevalier R. A., Frierson D. M., 2001, 563, 806
- Bodenheimer P., Sweigart A., 1968, *ApJ* 152, 515
- Boily C. M., Lynden-Bell D., 1995, *MNRAS*, 276, 133
- Bondi H., 1952, *MNRAS*, 112, 195
- Bonnor W. B., 1956, *MNRAS*, 116, 351
- Bouquet S., Feix M. R., Fijalkow E., Munier A., 1985, *ApJ*, 293, 494
- Cai M. J., Shu F. H., 2005, *ApJ*, 618, 438
- Chakrabarti S. K., 1989, *ApJ*, 347, 365
- Chakrabarti S. K., 1990, *MNRAS*, 246, 134
- Chandrasekhar S., 1957, *Stellar Structure*. Dover Publications, New York
- Cheng A. F., 1978, *ApJ*, 221, 320
- Chevalier R. A., 1982, *ApJ*, 258, 790
- Chevalier R. A., 1983, *ApJ*, 270, 554
- Chiueh T. H., Chou J. K., 1994, *ApJ*, 431, 380
- Choi M., Evans N. J., II, Gregersen E. M., Wang Y., 1995, *ApJ*, 448, 742
- Contopoulos I., Ciolek G. E., Königl A., 1998, *ApJ*, 504, 247
- Das T. K., Pendharkar J. K., Mitra S., 2003, *ApJ*, 592, 1078
- Del Zanna L., Amato E., Bucciantini N., 2004, 421, 1063
- Draine B. T., McKee C. F., 1993, *ARA&A*, 31, 373
- Ebert R., *Zs. Ap.*, 37, 217
- Emmering R. T., Chevalier R. A., 1987, 321, 334
- Fabian A. C., 1994, *ARA&A*, 32, 277
- Fabian A. C. et al., 2003, *MNRAS*, 344, L43
- Falgarone E., Pety J., Phillips T. G., 2001, *ApJ*, 555, 178
- Fan Y. Z., Wei D. M., Zhang B., 2004, *MNRAS*, 354, 1031
- Fillmore J. M., Goldreich P., 1984, *ApJ*, 284, 1
- Foster P. N., Chevalier R. A., 1993, *ApJ*, 416, 303
- Goldreich P., Weber S. V., 1980, 238, 991
- Gunn J. E., Gott III J. R., 1972, *ApJ*, 176, 1
- Hanawa T., Nakayama K., 1997, *ApJ*, 484, 238
- Hanawa T., Matsumoto T., 1999, *ApJ*, 521, 703
- Hanawa T., Matsumoto T., 2000, *PASJ*, 52, 241
- Harada T., Maeda H., Semelin B., 2003, *Phys. Rev. D*, 67, 084003
- Hartmann L., 1998, *Accretion Processes in Star Formation*, Cambridge University Press
- Harvey D. W., Wilner D. J., Myers P. C., Alves J. F., Chen H., 2001, *ApJ*, 563, 903

- Hayashi C., 1966, ARA&A, 4, 171
 Hennebelle P., 2003, A&A, 397, 381
 Hidalgo J. C., Mendoza S., 2005, Phys. Fluids, 17, 096101
 Hunter C., 1977, ApJ, 218, 834
 Hunter C., 1986, MNRAS, 223, 391
 Inutsuka S., Miyama S. M., 1992, ApJ, 388, 392
 Jordan D. W., Smith P., 1977, Nonlinear Ordinary Differential Equations. Oxford Univ. Press, Oxford
 Kawachi T., Hanawa T., 1998, PASJ, 50, 577
 Kennel C. F., Coroniti F. V., 1984, ApJ, 283, 694
 Klessen R. S., Burkert A., 2000, ApJS, 128, 287
 Krasnopolsky R., Königl A., 2002, ApJ, 580, 987
 Kwok S., 1982, ApJ, 258, 280
 Kwok S., 1985, AJ, 90, 49
 Kwok S., 1993, ARA&A, 31, 63
 Lai D., 2000, ApJ, 540, 946
 Lai D., Goldreich P., 2000, ApJ, 535, 402
 Landau L. D., Lifshitz E. M., 1959, Fluid Mechanics (New York: Pergamon)
 Larson R. B., 1969a, MNRAS, 145, 271
 Larson R. B., 1969b, MNRAS, 145, 405
 Lou Y. Q., 1992, ApJ, 397, L67
 Lou Y. Q., 1993a, ApJ, 414, 656
 Lou Y. Q., 1993b, ApJ, 418, 709
 Lou Y. Q., 1994a, ApJ, 428, L21
 Lou Y. Q., 1994b, ApSS, 219, 211
 Lou Y. Q., 1996, MNRAS, 279, 129
 Lou Y. Q., 1998, MNRAS, 294, 443
 Lou Y. Q., Shen Y., 2004, MNRAS, 348, 717
 Lou Y. Q., Gao Y., 2006, submitted
 Lyutikov M., 2002, Phys. Fluids, 14, 963
 Maeda H., Harada T., Iguchi H., Okuyama N., 2002, Progress of Theoretical Physics, 108, 819
 McKee C. F., Hollenbach D. J., 1980, ARA&A, 18, 219
 McKee C. F., Ostriker J. P., 1977, ApJ, 218, 148
 McLaughlin D. E., Pudritz R. E., 1997, ApJ, 476, 750
 Mészáros P., 2002, ARA&A, 40, 137
 Murakami M., Nishihara K., Hanawa T., 2004, ApJ, 607, 879
 Nakayama K., Shigeyama T., 2005, ApJ, 627, 310
 Navarro J. F., Frenk C. S., White S. D. M., 1997, ApJ, 490, 493
 Ori A., Piran T., 1988, MNRAS, 234, 821
 Osterbrock D. E., 1989, Astrophysics of Gaseous Nebulae and Active Galactic Nuclei, (Mill Vally: Calif)
 Ostriker E. C., Stone J. M., Gammie C. F., 2001, ApJ, 546, 980
 Ouyed R., Pudritz R. E., 1993, ApJ, 419, 255
 Parker E. N., 1963, Interplanetary Dynamical Processes (New York: Wiley)
 Penston M. V., 1969a, MNRAS, 144, 425
 Penston M. V., 1969b, MNRAS, 145, 457
 Perna R., Vietri M., 2002, ApJL, 569, 47
 Porter D. H., Pouquet A., Woodward P. R., 1994, Phys. Fluid, 6, 2133
 Priest E., 1982, Solar Magnetohydrodynamics (Dordrecht: Reidel)
 Ryu D., Vishniac E. J., 1987, ApJ, 313, 820
 Saito M., Sunada K., Kawabe R., Kitamura Y., Hirano N., 1999, ApJ, 518, 334
 Sarazin C. L., 1988, X-Ray Emission from Clusters of Galaxies. Cambridge University Press, Cambridge
 Scalo J., Vazquez-Semadeni E., Chappell D., Passot T., 1998, ApJ, 504, 835
 Sedov L. I., 1959, Similarity and Dimensional Methods in Mechanics (New York: Academic)
 Semelin B., Sanchez N., de Vega H. J., 2001, Phys. Rev. D, 63, 4005
 Shadmehri M., 2005, 356, 1429
 Shen Y., Lou Y. Q., 2004, ApJ, 611, L117
 Shu F. H., 1977, ApJ, 214, 488
 Shu F. H., 1992, The Physics of Astrophysics II: Gas Dynamics (New York: University Science Books)
 Shu F. H., Adams F. C., Lizano S., 1987, ARA&A, 25, 23
 Shu F. H., Lizano S., Galli D., Cantó J., Laughlin G., 2002, ApJ, 580, 969
 Spitzer L., Physical Processes in the Interstellar Medium. Wiley, New York
 Strömgren B., 1939, ApJ, 89, 256
 Suto Y., Silk J., 1988, ApJ, 326, 527
 Takahashi M., Rillet D., Fukumura K., Tsuruta S., 2002, ApJ, 572, 950
 Tanaka T., Washimi H., 2002, Science, 296, 321
 Terebey S., Shu F. H., Cassen P., 1984, ApJ, 286, 529
 Tilley D. A., Pudritz R. E., 2003, ApJ, 593, 426
 Tsai J. C., Hsu J. J. L., 1995, ApJ, 448, 774
 van der Swaluw E., Achterberg A., Gallant Y. A., Toth G., 2001, A&A, 380, 309
 Vishniac E. T., 1983, ApJ, 274, 152
 Wang W. G., Lou Y.-Q., 2006, MNRAS, submitted
 Whang Y. C., 1984, JGR., 89, 7367
 Whitworth A., Summers D., 1985, MNRAS, 214, 1
 Wolf S., Launhardt R., Henning T., 2003, ApJ, 592, 233
 Yahil A., 1983, ApJ, 265, 1047
 Yu C., Lou Y.-Q., 2005, MNRAS, 364, 1168
 Zhang B., Mészáros P., 2004, Intl J. Mod. Phys., 19, 2358
 Zhou S., Evans N. J., II, Kömpe C., Walmsley C. M., 1993, ApJ, 404, 232

APPENDIX A: DERIVATION OF MHD PERPENDICULAR SHOCK CONDITION

We have the following basic definitions and relations

$$\frac{\rho_2}{\rho_1} = X, \quad \frac{u_2}{u_1} = \frac{1}{X}, \quad \frac{p_2}{p_1} = X, \quad \frac{B_2}{B_1} = X, \quad M_1 = \frac{u_1}{a}.$$

Momentum conservation (30) can be written as

$$Xp_1 + X^2 B_1^2 / (8\pi) + \rho_1 u_1^2 / X = p_1 + B_1^2 / (8\pi) + \rho_1 u_1^2.$$

Using the following two relations

$$\rho_1 u_1^2 = \rho_1 a^2 \frac{u_1^2}{a^2} = p_1 M_1^2, \quad \frac{B_1^2}{8\pi} = \frac{p_1}{\beta_1},$$

the foregoing momentum equation becomes

$$Xp_1 + X^2 p_1 / \beta_1 + p_1 M_1^2 / X = p_1 + p_1 / \beta_1 + p_1 M_1^2,$$

or simply

$$X + X^2 / \beta_1 + M_1^2 / X = 1 + 1 / \beta_1 + M_1^2.$$

It then follows immediately that

$$(X - 1) + (X - 1)(X + 1) / \beta_1 = M_1^2 (X - 1) / X.$$

The degenerate case of $X - 1 = 0$ would be trivial. Removing this factor $X - 1$, we readily arrive at

$$1 + (X + 1)/\beta_1 = M_1^2/X \ .$$

This is the quadratic equation governing the density ratio X , exactly the same as equation (32) in the main text.

